Engineering Geology 307 (2022) 106774

Contents lists available at ScienceDirect

Engineering Geology

journal homepage: www.elsevier.com/locate/enggeo

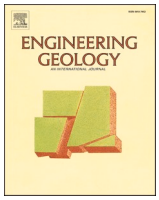

Dynamic numerical modelling of co-seismic landslides using the 3D distinct element method: Insights from the Balta rockslide (Romania)

Anne-Sophie Mreyen [a,*], Davide Donati [b], Davide Elmo [c], Frederic Victor Donze [d], Hans-Balder Havenith [e]

[a] Urban & Environmental Engineering, University of Liege, 4000 Liege, Belgium
[b] Department of Civil, Chemical, Environmental, and Materials Engineering, Université di Bologna, 40126 Bologna, Italy
[c] Norman B. Keevil Institue of Mining Engineering, University of British Columbia, Vancouver, BC V6T 1Z4, Canada
[d] ISTerre, Université Grenoble Alpes, 38400 Saint-Martin-d'Heres, France
[e] Department of Geology, University of Liege, 4000 Liege, Belgium

ARTICLE INFO

Keywords:
Flysch rockslide
Geomodelling
Slope reconstruction
Internal fracturing
Numerical modelling
Back-analysis

ABSTRACT

Ancient landslides of unknown origin can be found in large numbers in mountainous regions; some represent valid markers of (pre-)historic natural regimes referring to either long-term evolution or short-term peak events of climatic and seismotectonic nature. An example is represented by the Balta rockslide in the Romanian Carpathian Mountains. Its location in the seismically active Vrancea-Buzau region, as well as its morphological features, deep-seated rupture surface and large debris volume, raise the question of its failure history with regard to a possible co-seismic triggering. A 3D volume based reconstruction of the slope morphology together with field measurements of elasto-plastic in-situ rock properties allow to estimate pre-failure conditions of the slope, with special regards to the geological, i.e. flysch bedrock of poor to fair rock quality, and structural settings, i.e. anti-dip slope bedding crossed by the main joint family. The reconstructed slope behaviour was tested under static and dynamic forces with the 3D distinct element code 3DEC, subsequently used to simulate a failure scenario with a 120 s long real earthquake record that leads to the realistic post-failure morphology of Balta. For the latter, we observe a principally joint-controlled failure combined with internal fracturing of the undamaged rock mass. After 230 s of simulated time, the landslide debris reaches the valley bottom with maximum displacements of 1350 m and is marked by a lateral expansion to a broader extent than the source zone width, as observed in the field. Extension of this work to other pre-historic slope failures in the valleys of Vrancea-Buzau yield valuable new information for future seismic hazard estimations of the region.

1. Introduction

The characteristics, scale and effects of co-seismic landslides depend on multiple aspects that are linked to the energy of the associated seismic event and to the local settings of the affected rock slope (Keefer, 1984; Khazai and Sitar, 2004; Sassa, 1996; Romeo, 2000). Such factors comprise the shaking intensity of the seismic event, which depends on the epicentral distance, focal mechanism and depth, and the energy transmission to the slope, which is affected by the local geological, structural and morphological setting.

Various site-specific factors are known to intensify the seismic impact on slopes: (1) topographic effects, depending on the slope morphology in terms of geometry, curvature, and relief, can result in amplification of incident seismic waves (especially at slope and mountain crests; cf., Havenith et al., 2003b; Sepúlveda et al., 2005; Meunier et al., 2008; Huang et al., 2012; Maufroy et al., 2015), as well as directional site resonance and polarization effects (e.g., Burjánek et al., 2014; Del Gaudio et al., 2019; Weber et al., 2022); (2) geological and structural effects, comprising lithological predispositions (e.g., high impedance contrast between geological formations; cf., Bozzano et al., 2008; Bourdeau and Havenith, 2008; Luo et al., 2019) as well as structural settings (e.g., sliding prone dip angle and orientation of bedding planes or discontinuities, possibly coupled with reduced joint strength; cf., Willenberg et al., 2008; Stead and Wolter, 2015; Scholtès and Donzé, 2015); (3) weakened surface material, conditioned by micro- to macro-scale fracturing, weathering or long-term fatigue (cf., Moore

* Corresponding author.
E-mail address: as.mreyen@uliege.be (A.-S. Mreyen).

https://doi.org/10.1016/j.enggeo.2022.106774
Received 22 December 2021; Received in revised form 16 June 2022; Accepted 25 June 2022
Available online 16 July 2022

et al., 2011; Gischig et al., 2015; Burjánek et al., 2018); (4) hydrogeological regime changes as a result of intense precipitation events and fluctuating groundwater pressures as well as seismic-induced effects such as liquefaction (cf., Iverson et al., 1997; Wang and Sassa, 2003, 2009).

Geomechanical numerical modelling is an important tool to analyse the effects of seismic waves on a rock slope (e.g., Bozzano et al., 2008; Pal et al., 2012; Gischig et al., 2015, 2016; Song et al., 2020; Luo et al., 2020; He et al., 2020). Numerical simulations are largely applied in the analysis of anisotropic and jointed rock slopes (e.g., Kim et al., 2015; Bonilla-Sierra et al., 2015; Che et al., 2016; Li et al., 2019), taking into account the discontinuity of rock mass as an important factor for the overall slope stability, as they can be crucial for seismic wave propagation as well as amplification and polarization effects.

For (pre-)historic seismic landslides, the comprehension of interacting factors that are at the origin of the slope failure can be quite challenging. However, as outlined by Crozier (1992) and Jibson (1996), the study of paleoseismic landslides allows to better understand the paleoseismicity of a region, provided they can be dated and their co-seismic origin can be shown. In general, the failure history of ancient landslides in seismic regions is difficult to infer and extensive understanding of past interactions between seismic loads, geological-geomechanical conditions and local site effects is required. Various studies back-analyse the development of rock slope failures with a possible seismic history using numerical modelling techniques, such as Singeisen et al. (2020) for the 3.2 ka old Kandersteg rock avalanche, Swiss Alps, Bozzano et al. (2011) for the historic Scilla rock avalanche triggered by the 1783 Calabria earthquake, South Italy, or Zhu et al. (2019) for the seismically triggered Tahman paleolandslide in the eastern Pamir, Northwest China.

In this study, we analyze the Balta rockslide, a large paleo-landslide located in the flysch belt of the Carpathian Mountains of Romania, in the seismic region of Vrancea-Buzau (see Fig. 1), presenting morphological features that suggest a co-seismic origin (see description of study site in Section 2.2 about the landslide's source area, depth and volume). Furthermore, this site allows for an experimental approach of slope reconstruction to pre-failure conditions, and for testing factors in the static and dynamic domains that possibly led to the present-day slope shape. In regard to the seismic context of the region, we are particularly interested in the effects of dynamic simulations of the slope - in a broader perspective, the latter can help us to identify slopes such as Balta as marker of the pre-historic seismic activity of the Vrancea-Buzau region in Romania. In earlier works, Lemaire et al. (2020) studied the structural setting of the Balta slope, while Mreyen et al. (2021) analysed its geomorphic features and characterized the slide deposits as well as the in-situ sedimentary rock with geophysical methods. Here, we estimate a pre-failure state of the rock slope, i.e. prior to landsliding, and test the impact of seismic loading in realistic conditions with numerical modelling using 3DEC (3-dimensional distinct element code, version 5.2; Itasca, 2016).

2. Study area

2.1. Regional context

The study area is located in the Carpathian Flysch Belt, also called Flysch Carpathians, in the seismic region of Vrancea-Buzau. In the last centuries, the region produced several seismic events of magnitude 7 or larger; the best documented are the Vrancea earthquakes of the years 1802, 1838, 1940, and 1977 with estimated Mw 7.4 - 7.9 and intensities of I=IX-X MSK (e.g., Georgescu, 2002; Vacareanu and Ionescu, 2016; Rogozea et al., 2014). Fig. 1 shows the location of the study area in the vicinity of four historic Mw >7 epicenters, i.e. 1908, 1940, 1977 and 1986 with focal depths of 125 km, 150 km, 94 km, and 131 km, respectively. Focal mechanisms of these intermediate-depth events can be described as predominantly reverse (Radulian et al., 2018); the origin and nature of the seismic activity is highly discussed with the two suggested models being continental lithospheric delamination (Knapp et al., 2005) and descending oceanic lithosphere (Bokelmann and Rodler, 2014).

In terms of slope stability, Micu (2017) classifies landslide occurrence in the Flysch Carpathians into "high magnitude" events, i.e. deep-

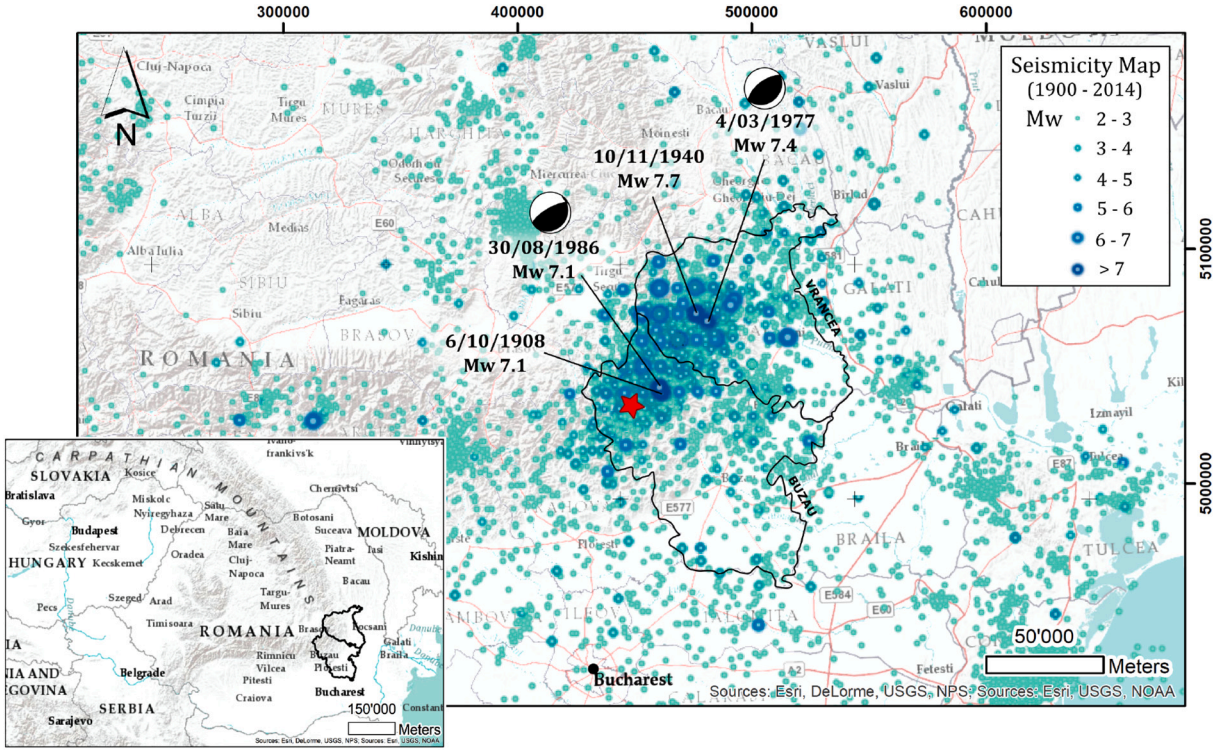

Fig. 1. Location of the study area (marked by red star) on a seismicity map of the Vrancea-Buzau region, Romania (after Mreyen et al., 2021).

seated rock block slides and rock slumps, and "low magnitude" events, i.e. shallow translational and rotational slides. In general, the region shows a good correlation between climatic peak events and landslide occurrences; as a consequence of a modest annual precipitation rate of 600-800 mm and thawing periods in late winter and early spring, mass movements occur in form of shallow slides, debris and mud flows (cf., Dragotă, 2006; Ministry of Environment, 2018; Micu et al., 2013). Distinct morphologies of deep-seated landslides of the area, such as Balta, represent large mass movements that differ from the seasonal slides of purely climatic origin. Could initial critical slope conditions in combination with powerful trigger events, such as seismic vibrations, have led to repeated or first time failure of these slopes? Historic reports of past earthquake events in the Vrancea zone mostly concentrate on structural damages and casualties in densely populated areas. Nonetheless, especially for the 1940 event, geohazards such as groundwater fluctuations, floods, liquefaction, wide and open cracks on slopes, as well as landslides have been documented (Radulescu, 1941; Radu and Spânoche, 1977; Georgescu and Pomonis, 2012; Mândrescu, 1981). As these historic records only cover the period of the last 200 years in isolated areas, investigations of proxies resulting from possible past seismic activity, such as mass movements, would contribute to the reconstruction of an extended regional seismic history, and thus support seismic hazard assessment in the Vrancea-Buzau region for longer periods.

2.2. Geomorphological and geological setting

The ancient Balta rockslide can be classified as rock rotational slide (after the classification of Hungr et al., 2014); Fig. 2 summarizes its geomorphological and structural setting. Similar to other deep-seated landslides situated in the Flysch Carpathians, it can be characterized as dormant and is covered by old forests and settlements (Micu, 2017); however, we do not dispose of any age records for Balta or other mass movements in the area. The north-facing rockslide is located on a slope crossed by a reverse fault (Fig. 2a) and presents features that hint at a possible co-seismic failure (Mreyen et al., 2021). One of these features is the morphology of the remarkable detachment scarp (Fig. 2b and d) in terms of steepness (mean slope angle of 40°, in the upper parts it even exceeds 50°), height (approximately 250 m), and amphitheatre shape, suggesting a powerful trigger event given the context of a rock slope. The head scarp furthermore shows an anti-dip slope bedding (Fig. 2e; i.e., geological layers dip into the slope, a characteristic that likely increases slope stability - in contrast to a dip slope, where layers dip into the valley) and is situated close to the crest of the mountain ridge, relatively far from the valley bottom. The scarp characteristics, together with the large body of debris that is still in place, mark the contrast to the numerous, mostly shallower, neighbouring landslides and flows (see contours in Fig. 2a). The studies of Mreyen et al. (2021) established a maximum depth of the landslide rupture surface at 70–90 m depth using a combination of active and passive seimic methods, and inferred a landslide volume of approximately 28.5–33.5 million m^3. The majority of the landslide debris accumulates in form of a plateau near the head scarp, where the landslide thickness reaches it maximum. The geophysical measurements highlighted the intense fracturing and fragmentation of the material constituting the landslide body, particularly within foot and toe, while more massive sandstone blocks can be found near the source area. Another interesting feature is the toe of the landslide body, that spreads out into the valley and supposedly deviated the original river course (Fig. 2b and c). As the opposite slope of Balta is also subject to former landsliding, a possible historic scenario of simultaneous failure of both slopes could have implied the formation of a landslide dam and a temporary barrier lake in the valley.

The slide developed in a Paleogene schistose sandstone flysch formation dominated by thick sandstone beds, apparent along the outcropping rupture zone (Fig. 2e) together with the anti-dip slope layering. The work of Lemaire et al. (2020) analysed the structural setting of the source rock mass with 40–50° inclined bedding planes towards S-SE (45/138; marked in red in Fig. 2f), and crossing discontinuities, i.e. two joint families, the first predominated by a Fisher mean plane of 56/331 and a secondary, with 74/223 (marked in green and blue in Fig. 2f, respectively). In general, the flysch rock properties of the study area can be described as weak (estimated GSI of 35–45 after Marinos et al., 2000); in comparison to the bedrock, the materials closer to the slope surface are characterized by very weak elastic properties (in terms of surface and P-wave velocity in the upper 50 m; for more details, see Section 4.1 and (Mreyen et al., 2021).

3. Slope reconstruction

Based on the volume of debris mass accumulated in the study area, an estimation of the Balta morphology prior to failure was realized using the established deterministic geomodel of the slope (Fig. 3a, where we distinguish between landslide mass and in-situ rock; see (Mreyen et al., 2021)). Various studies attempt reconstructions of pre-event morphologies, such as Singeisen et al. (2020) who used contour lines and point cloud interpolations in GIS software. Here, the slope reconstruction was performed using multiple 2D cross sections as input for surface mesh construction, and thus accounting for the final 3D volume balance of the slope by respecting a mass bulking factor of 15%, i.e. volume gain due to failure, computed similar to recommendations by Hungr and Evans (2004), Jaboyedoff et al. (2019). The used 3D volume balancing (difference of elevation models, cf., Zangerl et al., 2015) stands in contrast to the standard 2D volume balance cross section method using one single cross section for a respective site ("section area balance", cf., Zangerl et al., 2015). The reason for the application of the 3D volume balance method is the central source zone of the failure together with the lateral expansion of the landslide mass at the foot of the slope, i.e. mass motion is not exclusively downwards. In this case, we decided for a 3D reconstruction to establish a correct volume balance between the pre- and post-failure state of the slope (here, computed with the Leapfrog Geo software, Seequent, 2021). Fig. 3 shows three examples of the 2D cross sections, where the actual landslide mass is coloured in green, and the dotted line outlines the reconstructed topography. The section shown in Fig. 3a.1 marks the most pronounced central crest established in the reconstruction, whereas the defined slope angle diminishes towards West as shown in Fig. 3a.2. For sections crossing the lateral expansion of the landslide mass, the reconstructed topography results in a negative mass balance, i.e. the pre-failure slope estimates less mass to be in place than in its actual state (Fig. 3a.3). In total, 25 sections were used to create slope reconstruction curves; these latter were interpolated to a 25 m-resolution mesh, using the radial basis function (RBF) implemented in the Leapfrog software, that constitutes the modelled pre-failure topography. The reconstructed pre-failure topography displays a central N-S orientated ridge along which the maximum slope angle accounts for 54° (considering maximum slope angles of 55° in the area shown in Fig. 2a). A secondary ridge, oriented NE-SW, is implemented parallel to alignments of neighbouring mountain ridges (analysed using LiDAR digital elevation models of the studied region, see Fig. 2a). The landslide foot area was levelled to 400 m a.s.l, implying that the river valley was located south to the actual water course before slope failure. Fig. 3b displays the final reconstructed slope model that is used as input geometry for the numerical analysis described in the following section.

4. Numerical modelling

For the numerical analysis of the reconstructed slope, we used the three-dimensional distinct element code 3DEC developed by Itasca. In general, numerical analyses of natural slopes have been largely presented in the two-dimensional domain; however, three-dimensional analyses of natural slope behaviour are rather scarce, especially in a seismic context. Examples for the latter are recent studies of Luo et al. (2020), who analyse amplification effects over a natural slope affected

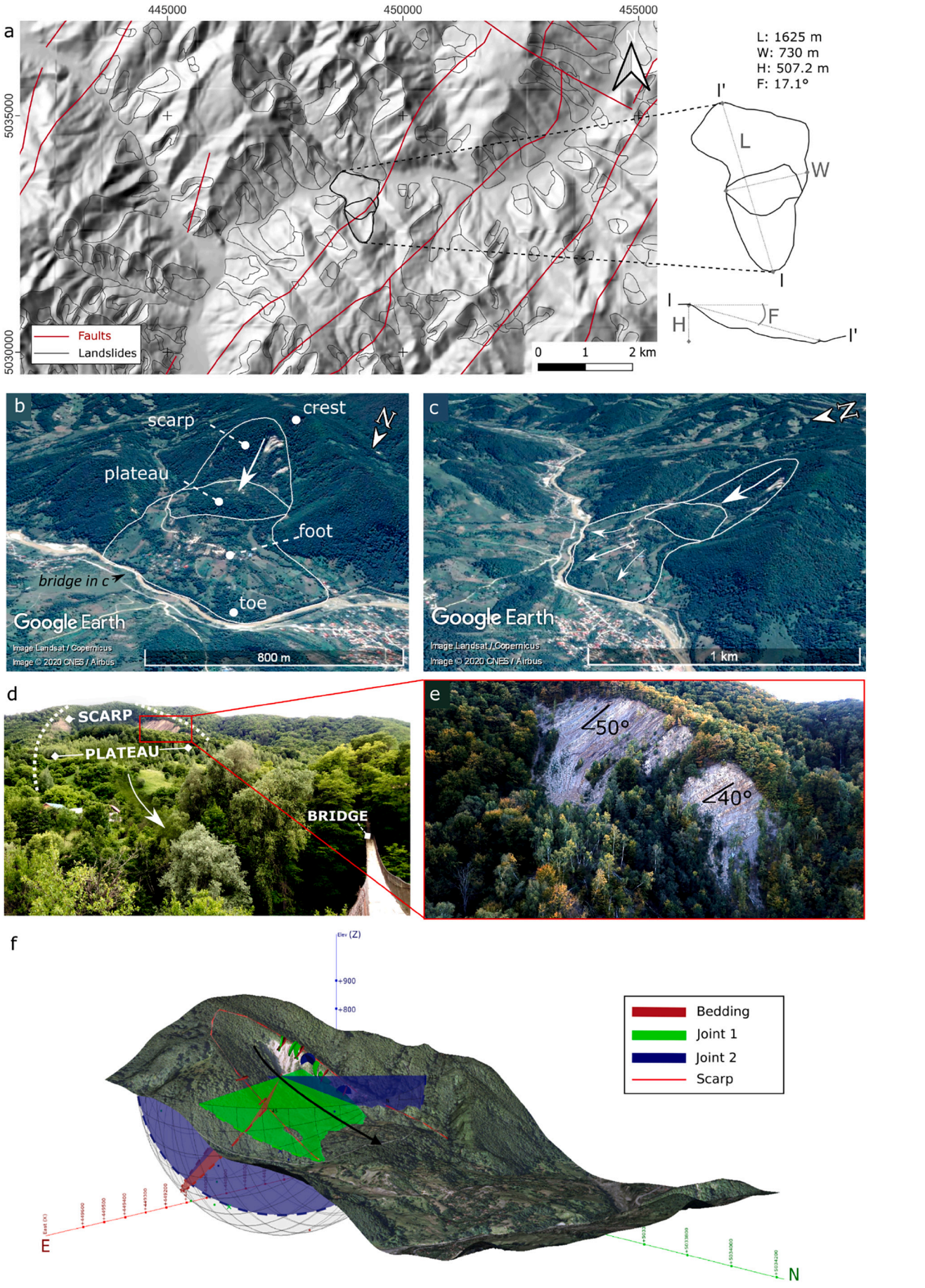

(caption on next page)

Fig. 2. (a) Hillshade of the study area: landslides are marked by black contours, faults by red lines (SW-NE aligned = reverse; NW-SE = strike-sklip); on the right, the outline and profile of Balta indicate its maximal length 'L', central width 'W', height 'H' and Fahrboeschung angle 'F'. Google Earth© imagery of the Balta rockslide: (b) geomorphic overview; (c) expansion and spread of landslide material marked by white arrows. Structural setting of the Balta rockslide: (d) photo taken from the valley in June 2017; (e) UAV image of the outcropping flysch bedding at the scarp after Mreyen et al. (2021); (f) structural model showing the flysch anti-dip slope bedding and crossing joint families after Lemaire et al. (2020).

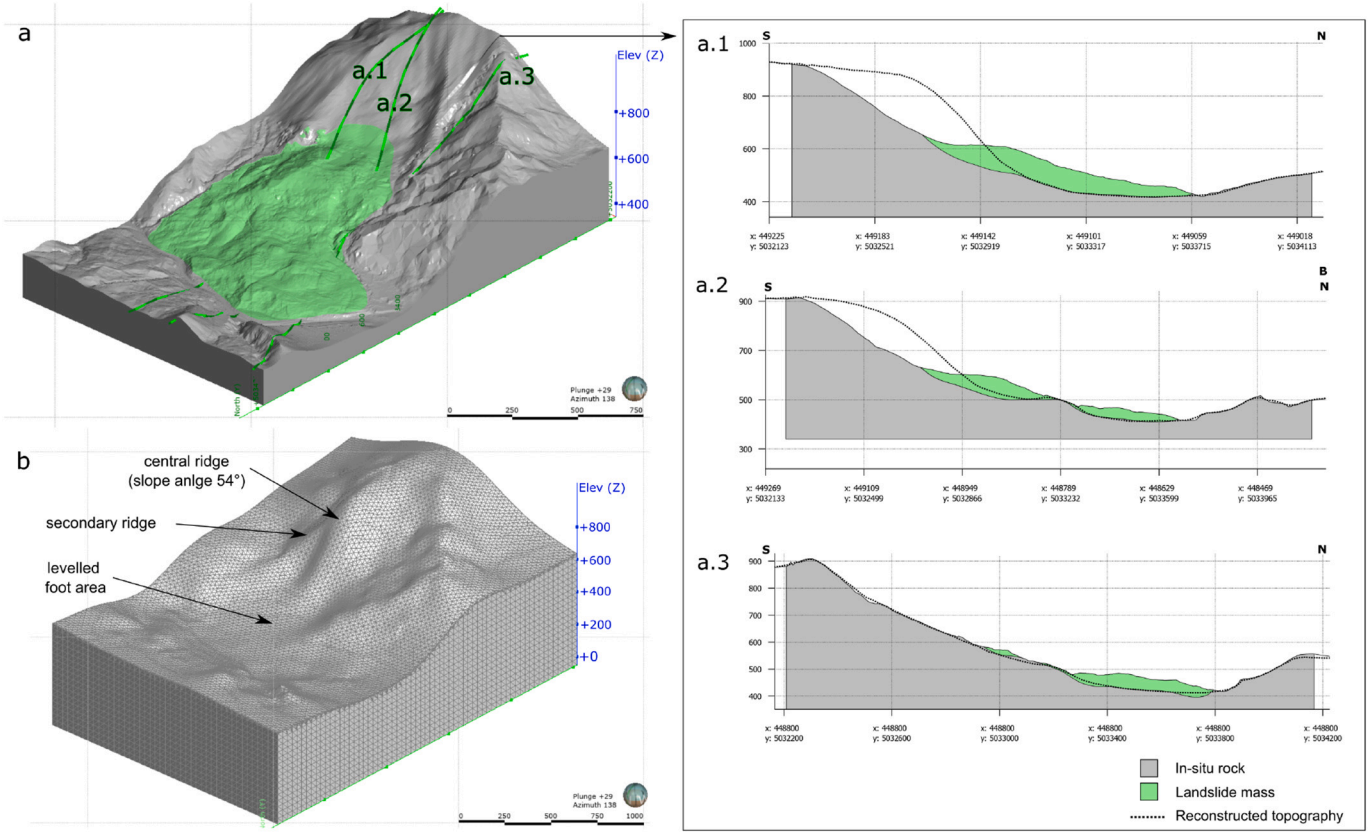

Fig. 3. Slope reconstruction of the Balta landslide: (a) actual, i.e. post-failure (presented in Mreyen et al., 2021), morphology with landslide mass marked in green - the three cross sections (a.1–3) show exemplary 2D reconstruction cruves; (b) reconstructed, i.e. pre-failure, morphology with surface mesh resolution of 25 m.

by seismic shaking in the visco-elastic domain with the 3D distinct element method, or Burjánek et al. (2019), who simulate 3D seismic wave propagation in a fractured rock mass using a finite-difference method. The necessity of a three-dimensional back-analysis of the Balta slope is given by its post-failure geometry that is marked by the rather narrow, but steep and profound, detachment scarp, while the relatively large volume of landslide sediments fans out into the valley (towards N), predominated by a lateral expansion (E-W orientated; Fig. 2c). The movement is thus presumed to be a three-dimensional problem, that due to the nature of debris distribution cannot be solved along a single section. To account for the particular morphological, geological and structural setting in conjunction with the seismic context of the study area, the presented analysis tests both static and dynamic forces. Calculations were performed on an Intel i7 2.7 GHz machine with 32 GB RAM; for the dynamic approach, computational costs were significant in terms of time with approximately 45 real minutes accounting for 1 simulated second (numerical time).

4.1. Setup of the numerical model

First, the pre-failure surface mesh created in LeapFrog was processed with Rhinoceros 5.0 (McNeel et al., 2010) and the Itasca plug-in Griddle 1.0 (Itasca, 2019). In Rhino, the lateral and basal surface boundaries of the 3D model were created and merged with the pre-failure morphology to create a closed 3D block model; another surface, that is later used to distinguish the weaker near-surface material (see, description of the study site and Mreyen et al., 2021), was modelled by duplicating the topographic mesh 50 m below its origin. Further structural elements, notably the rock bedding planes (see model composition shown in Fig. 6b), were also implemented in the CAD software to facilitate element discretization. By use of the Griddle plug-in, we created an unstructured surface and volume mesh within the model domain, formed by tetrahedral elements with edge lengths of 30 to 90 m, while the smallest elements are located close to the model surface to optimally emulate the topography. The created source area model was imported into 3DEC 5.2 (Itasca, 2016); it covers a surface of 1646 m width and 2400 m length and spans a vertical range of −50 to 992.4 m a.s.l. (see Fig. 4) with the model bottom fixed at a sufficiently large depth in order to guarantee full wave length transmission from bottom to top for the dynamic slope analysis. The model orientation is defined by the x-axis in E-W direction, y-axis in N-S direction and the vertical z-axis. Two discontinuity sets were introduced as interfaces between tetrahedra: the anti-dip slope bedding planes (implemented in Rhino; see inset figure in Fig. 4 and Fig. 6b) and a crossing joint family (created in 3DEC using the joint set function that cuts through blocks; see Fig. 6c). Distinct elements were made deformable by creating uniform finite-difference (FD) tetrahedral zones of 30 m and 12 m edge length within the polyhedron blocks (fixed according to Eq. (5)) for the undamaged bedrock and the near-surface, respectively. The resulting computational mesh is shown in Fig. 4 (see zoom on FD mesh).

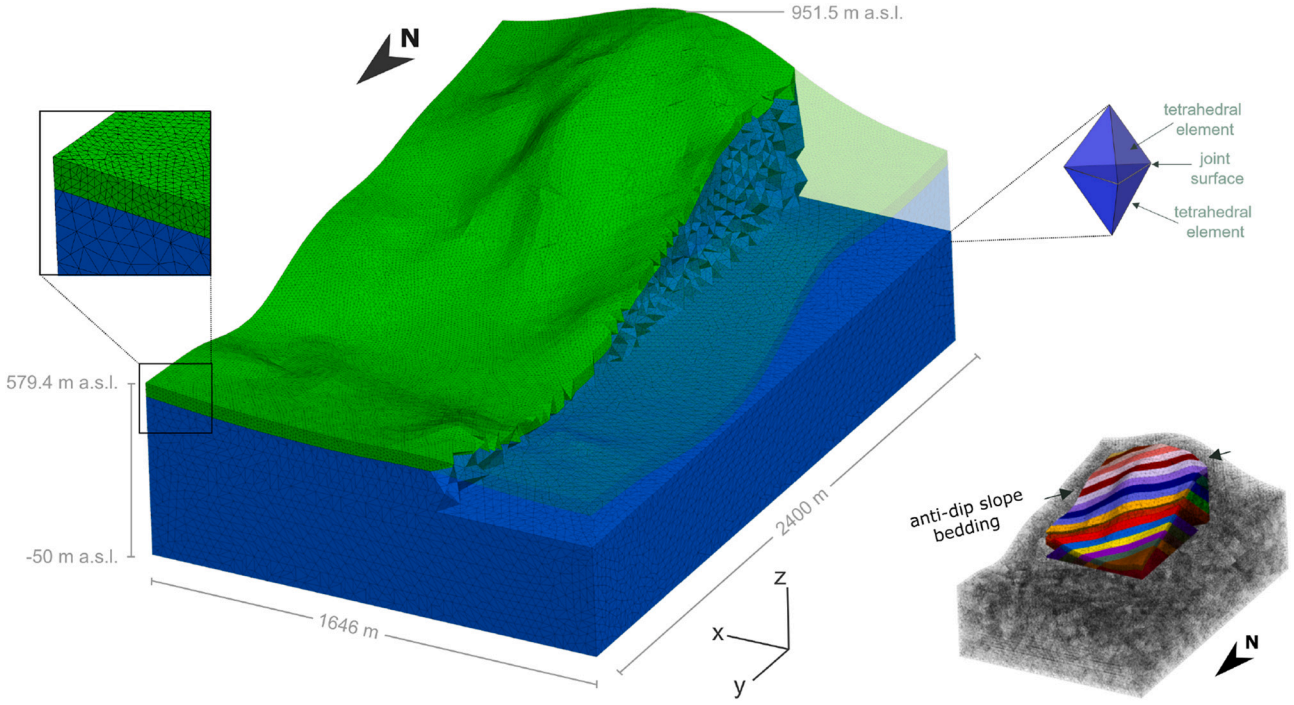

Fig. 4. Model setup of the Balta slope in 3DEC; green and blue differentiate the near-surface and undamaged bedrock material, respectively, with a FD zoning of 12 m and 30 m (zoom on the left). The inset figure in the lower right illustrates the modelled anti-dip slope layering of the flysch bedrock.

Table 1 lists the physical properties assigned to the rock block material; the elastic rock parameters were defined on the basis of the geophysical surveys performed in the study area, presented in Mreyen et al. (2021). Due to the lack of laboratory tests (given the challenge of extracting a rock sample adequate for geotechnical laboratory testing) and the scale discrepancy between laboratory and field conditions, the plastic rock mass parameters were indirectly derived using average rock properties for similar lithotypes (mi=15, UCS=75 MPa) provided in the RocLab software database (Rocscience, 2002), and considering a GSI of 35–45 (based on field observations, we associated the outcropping rock at the source zone to the flysch class B to C with good to fair surface conditions of discontinuities, afterMarinos and Hoek, 2001). The Hoek-Brown parameters were fitted to the Mohr-Coulomb criterion (M-C values in Table 1) using the RocLab software (Rocscience, 2002). Due to the rather weak and highly strained in-situ flysch bedrock and as observed for the landslide debris mass in the field, we aim to simulate fracturing of "undamaged" bedrock material, an approach that is revised by Donati et al. (2018) and applied, e.g., in the study of Gischig et al. (2015) simulating rock fatigue after repeated seismic stresses of a 2D slope using Voronoi tessellation. In our case, this approach allows to reproduce internal fracturing of the landslide material that takes into account the behaviour of the flysch rock mass itself next to the structural aspects of the slope. Block motion is thus not only enabled along the modelled discontinuities (i.e. flysch bedding plane and crossing joint set), but also in between at the interfaces of tetrahedral blocks (i.e. within the rock mass). For the discontinuities, the Coulomb slip failure criterion was applied; the strength properties, thus representing the defined joint structures as well as boundary conditions between blocks, are listed in Table 2. Note, the interfaces between tetrahedras were assigned the same properties as the discontinuity sets to account for the intense structural damage that characterizes the rock mass. The values assigned to the 50 m thick near-surface layer (see green layer in Fig. 4) account for the poor material and joint strength due to weathering effects and possibly tectonic fatigue, as observed by geophysical tests on in-situ rock in the study area (see Mreyen et al., 2021). Residual values are assigned by the system as soon as initial slip has occurred.

During numerical calculations, the kinematic behaviour of blocks is monitored along seven history points at the model surface and three history points inside the model. Each history point records displacement, velocity, and acceleration in the x-, y-, and z-directions (see Fig. 5).

In total, five different internal model structures were tested during the numerical analysis as illustrated in Fig. 6 along a 2D cross section of

Table 1
Elastic and Mohr-Coulomb (M-C) material parameters of the rock mass for the near-surface and the undamaged bedrock.

Rock mass		Near-surface	Undamaged bedrock
Elastic	Density ρ [kg/m^3]	2000	2400
	Young's modulus E [GPa]	1.7	10.7
	Bulk modulus K [GPa]	2.1	9.6
	Shear modulus G [GPa]	0.6	4.1
	Poisson's ratio ν [−]	0.37	0.31
	P-wave velocity V_P [m/s]	1200	2500
	S-wave velocity V_S [m/s]	550	1300
M-C	Cohesion C [MPa]	0.01	1
	Tensile strength σ_T [MPa]	0.005	0.5
	Internal friction angle φ°	42	45

Table 2
Strength properties of the discontinuities for the near-surface and the undamaged bedrock.

Discontinuities		Near-surface	Undamaged bedrock
Coulomb slip	Joint normal stiffness Jk_N [GPa/m]	0.1	1
	Joint shear stiffness Jk_S [GPa/m]	0.05	0.5
	Cohesion c [kPa]	5	10
	Residual cohesion c_r [kPa]	0	0
	Tensile strength T [kPa]	0.1	1
	Residual tensile strength T_r [kPa]	0	0
	Friction angle ϕ°	40	42
	Residual friction angle ϕ_r°	28	30

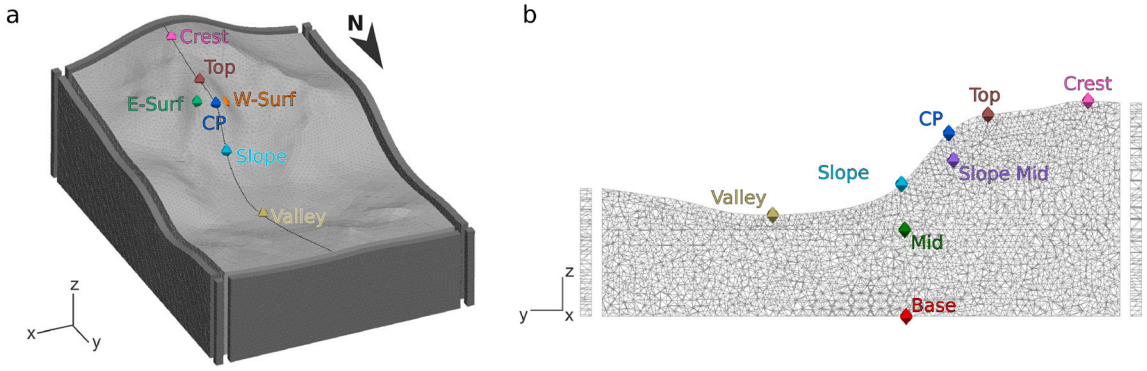

Fig. 5. Position of history points at the model surface (a) and within the model (b); the position of cross section is marked by the projected line in (a). The plane grids and corner columns around the model block illustrate free-field boundaries used in the dynamic analysis (see Itasca, 2016).

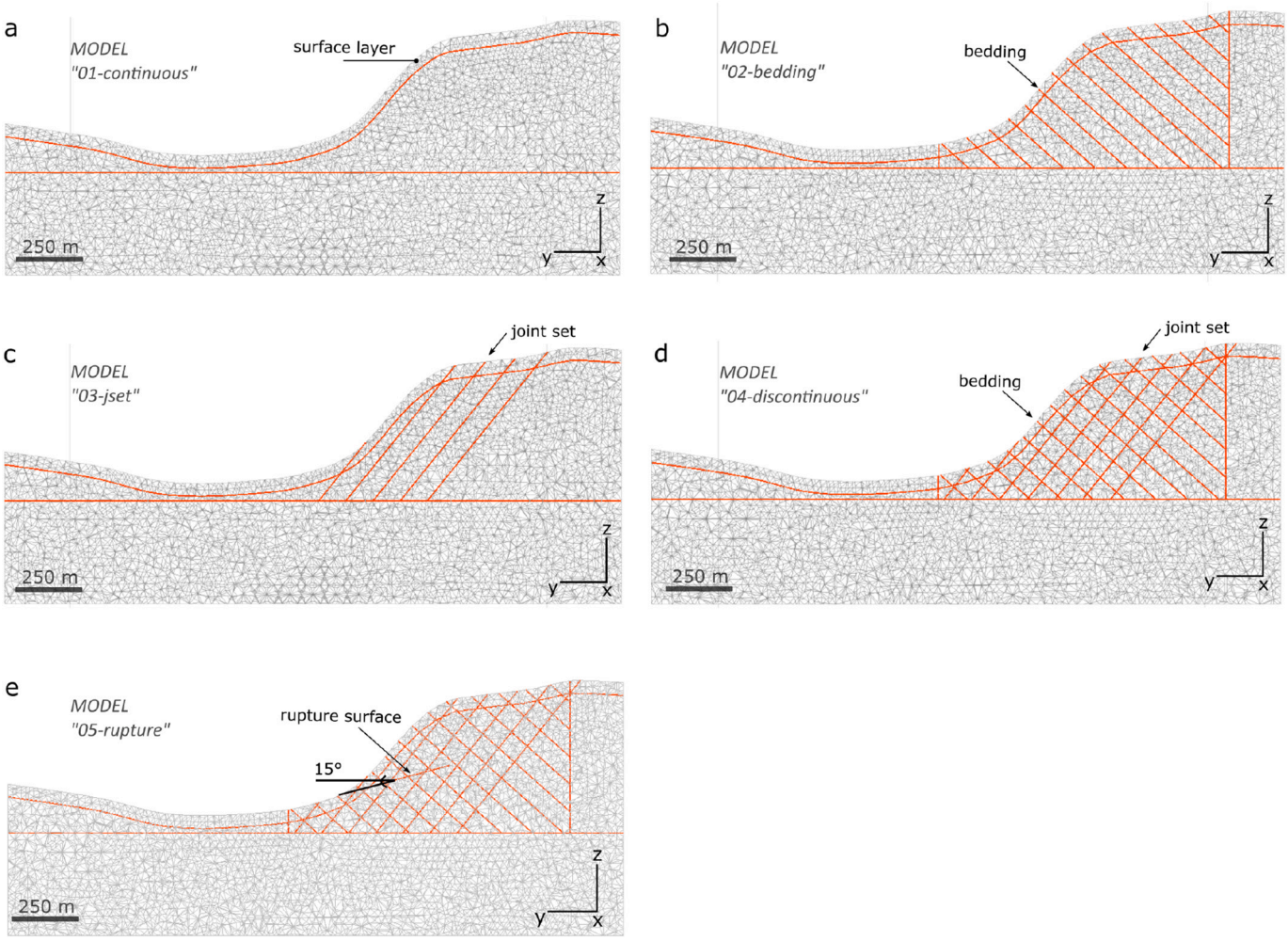

Fig. 6. Cross section of the structural model configurations with continuous rock mass (a; *01-continuous*), with implemented flysch bedding planes only (b; *02-bedding*), with joint set only (c; *03-jset*), and setup with bedding planes and crossing joint set combined (d; *04-discontinuous*, see inset figure in Fig. 4), with modelled auxiliary rupture surface (e; *05-rupture*). Note, the near-surface layer pointed out in (a) was modelled in all configurations and represents the weaker material and joint strength at the slope surface (see Tab. 1 and 2).

the slope. The complexity of model structure was progressively increased during the modelling process as they depend on computational capacities. The basic structure on which all models build on, i.e. the *01-continuous*, consists of the slope material (undamaged bedrock) and the near-surface material presenting weaker material strength (Fig. 6a). The other structures (Fig. 6b-d) intend to analyse, separately and jointly, the effect of bedding planes (*02-bedding*) and joint sets (*03-jset*) in the slope; model *04-discontinuous* (Fig. 6d) combines both discontinuity configurations. Dip angles and orientations of discontinuities were assigned in accordance to the field measurements Lemaire et al. (2020, presented in][]. In model structure *05-rupture* (Fig. 6e), an additional discontinuity, i.e. an auxiliary rupture zone, modelled as joint

plane crossing blocks was included. Such feature was introduced to avoid unrealistic self-stabilization behavior of the slope, due to interlocking of tetrahedra, and thus to facilitate initial detachment of rock mass. A similar approach has been applied by Havenith et al. (2003a) and Gischig et al. (2016) in the 2D domain. The pre-determined rupture surface was implemented with a dip of 15° in slope direction, while the strength properties assigned to the plane account for a superior joint friction angle, i.e. ϕ of 20°, and a residual ϕ of 17.5°; strength reduction along the joint plane is only enabled after initialization of block motion (using the residual geomechanical parameters).

4.2. Static conditions

The static modelling domain seeks a (non-inertial) model solution of static force-equilibrium under gravitational forces as well as in-situ and applied stresses. In our simulations, only gravitational stresses were considered, while no other natural in-situ stresses were assumed to have an influence on the slope behaviour. The boundary conditions chosen for the static model domain fix the velocity normal to the boundaries (lateral borders and bottom of the model). The static equilibrium state is measured with the maximum out-of-balance force, i.e. the net nodal force vector at each gridpoint of block, compared to the total applied forces. In a first stage, models were run to a static equilibrium (i.e. unbalanced force ratio $<10^{-5}$) under gravity loading (f_z = -9.81 m/s^2); auto damping was applied and mass scaling was enabled.

A strength reduction analysis of block material and joint surfaces was performed for the geomechanical parameters that quantify plastic deformation. This analysis evaluates the sensitivity of the chosen values in terms of static slope stability with the factor of safety (FoS). The FoS solution implemented in the Itasca codes uses the strength reduction method that is commonly applied in slope stability analyses; it is based on the Mohr-Coulomb failure criterion and the Coulomb-slip model employing a progressive reduction of material or joint strength until failure occurs.

The strength reduction thereby concentrates on the parameters of cohesion C and friction angle φ (separately or combined) according to:

$$C^{\text{trial}} = \frac{1}{\text{FoS}^{\text{trial}}} \; C \tag{1}$$

and

$$\varphi^{\text{trial}} = arctan\left(\frac{1}{\text{FoS}^{\text{trial}}} \; tan\varphi\right) \tag{2}$$

where the superscript *trial* designates the trial values used during the strength reduction calculations.

The bracketing approach implemented in the software uses a similar technique to Dawson et al. (1999) that determines initial stable and unstable bracketing states for the system. These brackets are then progressively narrowed by reducing the space between stable and unstable solutions below a specified tolerance (default value of 0.005); as a result, a stable or unstable solution is found. The number of used solution cycles thereby varies according to the characteristic response time of the model (depending on the assigned material strength). Over one averaged current span of cycles, a mean value of force ratio is calculated and compared with the mean force ratio of the previous span of cycles; the cycling stops when the bracketing tolerance is reached, otherwise another loop is executed. The stable solution designates a system in equilibrium state, while an unstable solution indicates a system in continuing motion. In a static analysis, for a system at zero stress rate (i.e. no external stresses are applied), only gravity is considered as system load during FoS calculations.

For this analysis, we used the basis model structure (Fig. 6a) with uniform slope material in order to test the sensitivity of the selected model parameter; calculations were performed within a range of 25% of the peak and residual values, respectively.

4.3. Dynamic conditions

The dynamic modelling domain aims for a model solution under dynamic loads that generate and dissipate kinematic energy for a short duration and high frequency (e.g., seismic or explosive loads). Two different boundary conditions are used for the model bottom and lateral boundaries, i.e. viscous and free-field conditions, respectively. At the lateral model boundaries, we define boundary conditions that account for free-field motion without lateral constraints (infinite model, see illustration in Fig. 5). The latter, originally introduced by Cundall et al. (1980), allows upwards propagating energy to fully move as plane wave without being absorbed at the model boundaries. A non-reflecting viscous boundary is applied at the model base as it uses independent absorption points at the model borders, i.e. scattering of outgoing wave energy back inside the model is suppressed (Lysmer and Kuhlemeyer, 1969). For dynamic calculations, a common approach to overcome non-reflecting boundaries at the model bottom is the conversion of basal input motions into stress boundary conditions according to:

$$\sigma_n(t) = 2\rho V_P C_n(t) \tag{3}$$

and

$$\sigma_S(t) = 2\rho V_S C_S(t) \tag{4}$$

where σ_n and σ_S are the applied time-dependent normal and shear stresses, ρ the mass density, and V_P and V_S the P-wave and S-wave propagation velocities through the medium, respectively. C_n and C_S represent the input normal and shear velocities, respectively.

In this regard, the finite-difference (FD) element size is defined following the law of Kuhlemeyer and Lysmer (1973) to guarantee accurate numeric wave transmission through the medium according to:

$$\Delta l \leq \frac{\lambda}{10} \quad \text{to} \quad \frac{\lambda}{8} \tag{5}$$

where Δl is the FD spatial element size and λ the wavelength associated with the highest frequency component of input wave. For the presented models, the latter relation enables a complete energy transmission in the frequency range of 1.8 to 5.5 Hz for the chosen FD element size of 30 m, for the undamaged bedrock, and 12 m for the near-surface.

A common approach for synthetic reproduction of earthquake signals is the Ricker wavelet which is able to approximate the spectral content of recorded earthquake signals (Gholamy and Kreinovich, 2014). The function was introduced by Ricker (1953) as follows:

$$A = (1 - 2\pi^2 f^2 t^2) \; e^{-\pi^2 f^2 t^2} \tag{6}$$

where A is the amplitude, f the central frequency and t the time.

In the frame of this work, a synthetic Ricker multiplier that combines a low- and a high-frequency part, notably with the central frequencies 1.4 and 3.5 Hz, was used to test the seismic loading of the Balta slope. The signal is applied at the model base as stress-time history during three excitation sequences (total duration of 14 seconds). The applied stress amplitude is 1 MPa in x- and y-directions, reproducing a shear stress in lateral directions. The energy transmission of the synthetic wavelet is monitored at the history points introduced in the model domain in terms of velocity and acceleration against time; the applied stress results in an input acceleration of 1 m/s^2 at the model base, i.e. approximately 0.1g.

The effect of ground shaking on the modelled Balta pre-failure slope was also tested using a real event record. As we had no access to local Vrancea M >7 intermediate depth earthquake records, we decided to use a subduction model to represent seismic activity in Vrancea (as suggested by, e.g., Bokelmann and Rodler, 2014). We selected a significant seismic event that occurred in another tectonically active region of higher intensity and lower depth, namely the 2014 Iquique earthquake (Chile), an offshore M_W 8.2 earthquake caused by the convergence the

Nazca and South America plates (Pi na-Valdés et al., 2018; USGS, 2020). We numerically control the intensity of the introduced dynamic record by testing different stress magnitudes, and by verifying the slope model response in terms of PGA, aiming for responses comparable to those produced by the synthetic Ricker signal. However, we do not control frequency contents or spectral characteristics of the applied signal, which might differ from the original study location. The data used for our simulations was recorded 170.2 km distant from the epicenter (Chusmiza station, National Seismic Network of Chile); the input signal is shown in Fig. 7 in terms of applied velocity and acceleration. The earthquake record was implemented at the model bottom as stress-time history in x- and y-direction (representing upwards propagating shear stresses) during 120 seconds.

The mechanical damping applied in a dynamic analysis should account for the energy loss in the natural system during dynamic loading, while for a natural ground (soils and rocks), damping can be considered as frequency-independent (Cundall, 1976). Rayleigh damping offers a numerical solution to overcome this limitation and provides a approximately hysteretic solution over a defined frequency range (Bathe et al., 1975; Biggs, 1964); here, a Rayleigh damping of 2% is applied (for geological materials a Rayleigh damping of 2–5% is recommended, see, Biggs, 1964).

In order to quantify the site effects of the modelled Balta slope, we computed standard spectral ratios (SSR) of acceleration records between two points of the model domain with seismic Ricker loading. The numerical SSR's compare the signal response of the original input wave (here, at the model basis) with the signal response at a chosen history point (here, at the model surface) in the frequency domain. Such analysis is applied in multiple numerical studies to quantify the site effects of landslide prone slopes, e.g., Havenith et al. (2002); Gischig et al. (2015); Luo et al. (2020). The SSR analysis was performed for two case scenarios, i.e. SSR01 that was constructed with undamaged bedrock material ('1-material'), and SSR02 that uses both, near-surface and undamaged bedrock material ('2-material'; see Tab. 1). For the SSR analyses, the dynamic input was modelled with a shear stress propagating from the model bottom upwards in y-direction (i.e. N-S, direction of the slope) and in x-direction (i.e. E-W). The acceleration record at the model base was used as artificial reference station (signal amplitudes multiplied by two); the reference signal is compared to the record at the slope surface and top (see Fig. 5; history points 'slope' and 'top'). For the spectral analysis, three constant time windows of 5–10 seconds length were chosen per signal, allowing for a maximum time window overlap of 50%. The final SSR curve was geometrically averaged from the individual curves and standard deviations were calculated.

5. Results

5.1. Static strength reduction analysis

For all models, a static solution was obtained with the used input parameters; the slope is considered as initially stable and does not suggest failure in its in-situ conditions. The static model response was tested in terms of joint strength with elastic block material. As shown in Fig. 8a, the static model exclusively responds to changes of the joint's friction angle ϕ. While the overall slope is evaluated with a FoS of 2.23 with $\phi = 42°$ (used for the undamaged bedrock material in our simulations), its stability decreases to a FoS of 1.32 with $\phi = 28°$ (used for the surface material in our simulations). By decreasing ϕ to 21°, i.e. 28° reduced by 25%, the overall slope is classified as unstable (FoS = 0.95). For the variations in joint cohesion c (using a constant ϕ of 42°), the slope shows a FoS of 2.23 for all calculations, demonstrating that the joint strength is conditioned by the selected ϕ.

The sensitivity of material parameters was evaluated in terms of block internal cohesion C and internal friction angle φ. For these tests, the Mohr-Coulomb criterion and a constant joint friction angle ϕ of 30° were chosen. As shown in Fig. 8b, the FoS calculations of the material variations all show the constant result of 1.51 (with a negligible decrease to 1.49 for the minimum value of internal block cohesion). Again, the FoS result of 1.51 is controlled by the joint friction angle ϕ of 30° rather than by the varied material strength.

5.2. Ground acceleration and amplification analysis

Based on the initial stress state of the model, the slope model is analysed in terms of dynamic wave transmission that simulates ground acceleration. Here, the excitation with the Ricker input signal accounts for the elastic response of the slope; results are shown in Fig. 9 for the two scenarios of the *01-continuous* model configuration (see Fig. 6a), i.e. the uniform material model of bedrock and a layered model with a surface-near weaker material (that was observed in the field and is used herein for the failure simulations). The uniform model reaches a PGA of 0.35g and 0.2g in y- and x-direction, respectively, at the model surface (recorded at the history point 'top', see locations in Fig. 5). The two-layered model produces PGA values of 0.5g and 0.4g in y- and x-direction, respectively; the implication of a surface-near layer with reduced material strength results thus in more pronounced acceleration values at the slope surface.

The numerical computation of standard spectral ratios between two reference points in the model (notably the model base vs slope surface 'slope' and crest 'top', see history point locations in Fig. 5) is used to further analyse the dynamic amplification potential of the reconstructed slope. The amplification as a result of y- and x-orientated excitation is presented in the frequency-domain (see Fig. 10a and b, respectively) for the one-layered (uniform bedrock material, i.e. SSR01) and the two-layered (with surface-near weaker material, i.e. SSR02) material models.

For the y-orientated excitation (Fig. 10a), we notice a topographic effect by comparing the slope and top receiver response of the uniform material model, with an increase of the averaged amplification value from 2 to 5.5 in the frequency range 0.8–1 Hz. The material contrast of the 2-material model furthermore provokes pronounced amplification at the slope and top in the frequency range 5–8 Hz, as well as 1.5–2 Hz for the top receiver. The x-orientated excitation (Fig. 10b) shows similar

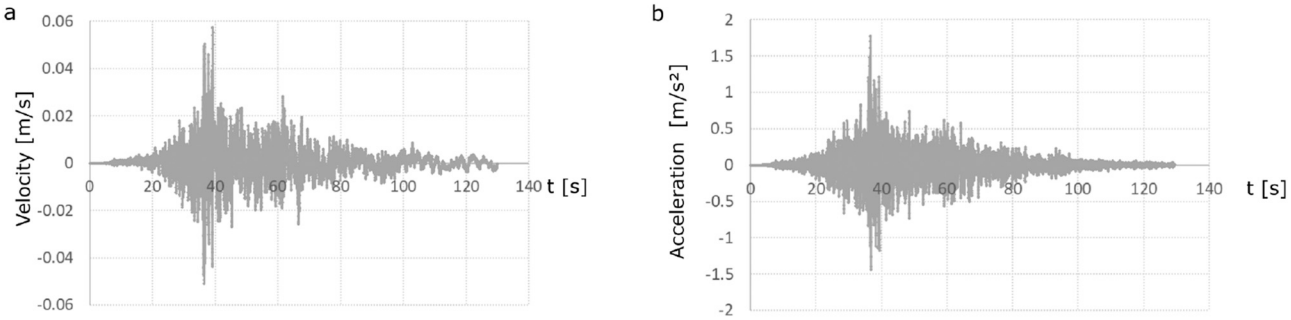

Fig. 7. 2014 Iquique event: (a) velocity and (b) acceleration record used for the dynamic loading of the reconstructed Balta slope.

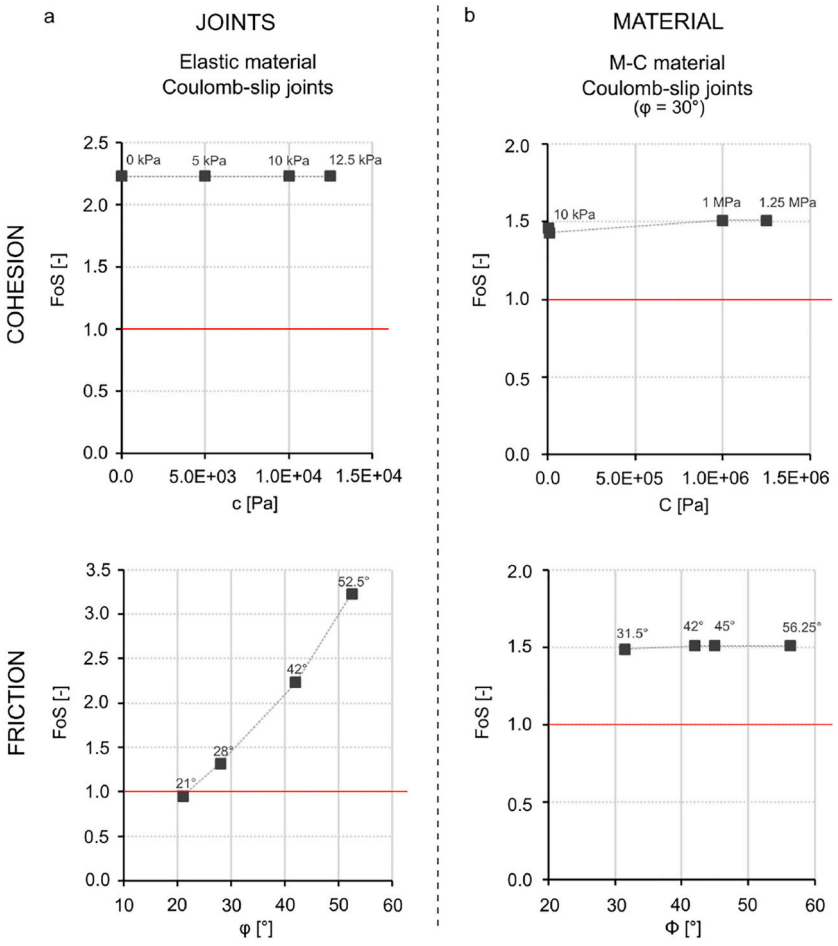

Fig. 8. Strength reduction analysis of plastic parameters of joints (a) and block material (b).

amplification patterns in the lower frequency range (0.8–2 Hz), while the addition of a second material shows less effects for frequencies >5 Hz than for the y-excitation. Note, the amplification results of both scenarios at the top receiver in the frequency range of 0.8–1.2 Hz have been observed by actual measurements that we performed at the crest and analysed in terms of HVSR (presented in Mreyen et al., 2021), validating the numerically produced results at the top in the lower frequency range.

5.3. Reproduction of slope failure

Subsequently to the analyses of the model behaviour to gravitational and dynamic stresses, we intend to reproduce the failure state of the Balta rockslide with seismic loading. In a first state, we tested the latter with the implemented model structures *03-jset* and *04-discontinuous* (see Fig. 6c and d, respectively), using the beforehand introduced Ricker excitation (Eq. (6)) as well as the earthquake record of the 2014 Iquique event (Chile; Fig. 7) that simulates a thrust event of intermediate depth. In Fig. 11, we show the models after 14 s of ground motion (three successive Ricker wavelets in x- and y-direction, producing PGA values of 0.1 to 0.2 g at the model surface) with a changed displacement pattern for the two different structural configurations (note, the colour legends in Fig. 11 do not display maximum values, but were set to the same values per column to enhance comparison between both model configurations). The *03-jset* model, with joint set only, shows the most pronounced values at the frontal part of the slope, with a maximum y-displacement of 15.19 m and x-displacement of 4.07 m (recorded at the history point 'CP', see Fig. 5). At the history point 'slope mid', 100 m below slope surface, the maximum displacement magnitude reaches only 0.2 m. The *04-discontinuous* model triggers block motion in larger depth, showing the impact of the implemented bedrock bedding planes; y- and x-displacements recorded at 'CP' are 23.23 m and 4.37 m, respectively, while maximum x-displacement is reached at the eastern slope surface ('E-Surf') with 9.02 m.

In both models *03-jset* and *04-discontinuous*, a natural sliding surface could not be initiated and a block detachment leading to massive slope failure could not be reached under dynamic loading. To overcome the numerical limitations, we continued the analysis with the model structure *05-rupture* (introduced in the description of model setup; see Fig. 6e), that comprises the structural elements of *04-discontinuous* together with an additional auxiliary rupture surface of 15° inclination in slope direction. The model structure was tested beforehand under static conditions reaching a static equilibrium state and allowing for further dynamic analyses. In the following we present the dynamic results for both, Ricker excitation (total of 60 simulated seconds) and earthquake simulation (total of 230 simulated seconds), using the model structure *05-rupture*.

5.3.1. Ricker excitation

The triple Ricker wavelet excitation was introduced at the model base in x- and y-direction. The total duration of cycling was set to 60 seconds of which the first 14 seconds account for the dynamic input duration (i.e. simulated time, calculated by the time step of one numerical cycle); block displacement, velocity and acceleration are recorded at the defined history points. The critical time of first block detachment is monitored by the shear displacement along the rupture surface using two history points: a first history point is located at 15 m (i.e. in the near-surface layer), and a second at 250 m from the model

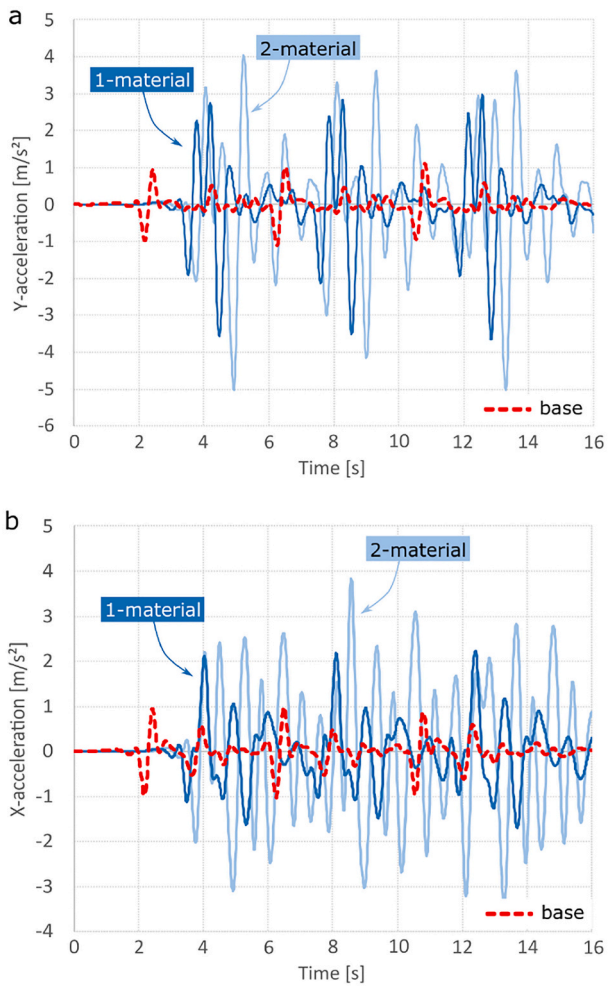

Fig. 9. Elastic model response of the *01-continuous* model configuration (see Fig. 6a) in terms of (a) y-acceleration and (b) x-acceleration at the model base (red curve) and model top (blue curves; see history point locations in Fig. 5). The 1-material test refers to a uniform bedrock material model; the 2-material test adds the near-surface material with weaker properties in the upper 50 m (see Table 1).

surface along the auxiliary joint plane. For the shear displacement along the sliding horizon, a first block detachment is recorded after 1.2 seconds (shear displacement of 0.15 m) at the surface near history point, and after 9.3 seconds (shear displacement of 9.92 m) at the second point; i.e. in comparison to the undamaged bedrock, failure of the weaker near-surface layer initiates after a relatively short period of seismic vibrations.

In Fig. 12, y-displacement of blocks is shown along a cross section at different stages. After the synthetic Ricker loading (first 14 simulated seconds), the layer limited by the first joint plane is completely detached and forms an initial scarp of approximately 15 m height (Fig. 12e). The initial failure can be characterized as shear dominated, while tension driven failure of blocks is only secondary. With further cycling, the blocks stay in motion due to the residual velocity of blocks. After the triggering of the first block layer, we notice the dragging of the second block layer due to the mass movement and the collateral stability reduction at the top and foot of the layer. After 60 seconds of cycling (i.e. simulated time), an initial detachment scarp height of approximately 150 m is produced (Fig. 12i), approaching the actual scarp height of 250 m of the Balta rockslide. Maximum displacement occurred at the history point 'CP', which is the point of highest curvature at the slope surface (see location in Fig. 5), with a total displacement magnitude of 423.03 m (of which 327.18 m account for y-displacement, i.e. in slope direction, 109.28 m for x-displacement, i.e. E-W, and 244.87 m for negative z-displacement, i.e. downwards). The highest velocity magnitude was reached at 'CP', while maximum acceleration were measured at the history point 'E-Surf' that monitors kinematic behaviour at the eastern slope surface.

5.3.2. *Earthquake simulation*

The Iquique earthquake record (Fig. 7) was introduced at the model basis in x- and y-direction with a duration of 120 seconds and model computations were maintained during additional 110 seconds (numerical time). Fig. 13 shows the total displacement magnitude of blocks after 230 seconds (inset figure) as well as the result of block motion along a central cross section during different cycling periods (note, seconds relate to the simulated time). A first detachment scarp is visible after approximately 10 seconds of induced seismicity and a superficial layer of rock collapses during the first 60 seconds of ground acceleration. In the course of this collapse, the material bulges up at the central part of the slope, before running down to the valley. The failure of underlying block layers initiate at the foot of the modelled sliding plane, while motion also accentuates at the upper front of the slope. We also notice expulsion of smaller blocks along the sliding plane and fracturing of the material during their down slope displacement. Recorded maximum displacements accentuate at the 'CP' history point (see location in Fig. 5) with a three-component magnitude of 925.9 m (absolute values of 94.9 m, 857.2 m and 344.2 m in x-, y-, and z-direction, respectively). Maximum x-displacement was recorded at the eastern slope flank with 342.21 m at the history point of the eastern slope flank 'E-surf' as well as highest peak acceleration. Highest velocity occurred at the history point of the western slope flank 'W-Surf', i.e. the surface point of the western slope flank.

A large mass of debris reached the valley after a total cycling duration of 120 seconds. Furthermore we observe a pronounced lateral spread of material (see inset figure in Fig. 13); the eastern slope flank tends to collapse in a purely eastwards motion, before the debris runs out towards the valley to the NE, while the western slope seems to be predominated by a NW-orientated motion.

Subsequent mass movement was observed during the additional seconds after ground acceleration as a result from residual block velocity; especially the inner slope and slope top (history points 'slope mid' and 'top') are subject to these entrainments with an increased velocity magnitudes during 60–80 sec after the initial ground acceleration. In Fig. 13 the slope morphology is shown along a central cross section for three different stages of cycling; the morphology is marked by the additional downhill orientated motion of blocks as well as the material bulging below the scarp and at the middle part of the slope; here, we also observe the fracturing of the material at the landslide basis, i.e. the former slope surface, resulting in a larger thickness of collapsed material in addition to the source zone's debris. The final modelled landslide thickness reaches values of 85–95 m. The scarp formation follows the inclination of the modelled joint planes and reaches a height of approximately 200 m after 230 s of cycling, approaching its actual height of 250 m.

6. Discussion

For the slope reconstruction of Balta, we used a three-dimensional volume balancing approach that proved efficient, nevertheless also presents uncertainties, i.e. other than the determined landslide volume, we have no quantifiable control over the original morphology prior to landsliding. We can only estimate, on the one hand, the material loss as a consequence to slope and river erosion, and on the other hand, the volume expansion as a cause of material detachment (expressed in terms of bulking factor). The presented solution is one out of multiple possible scenarios; nevertheless, we consider the chosen pre-failure model to be representative, since it allows to understand the relation of in-situ geomechanical properties and structural settings that were derived from

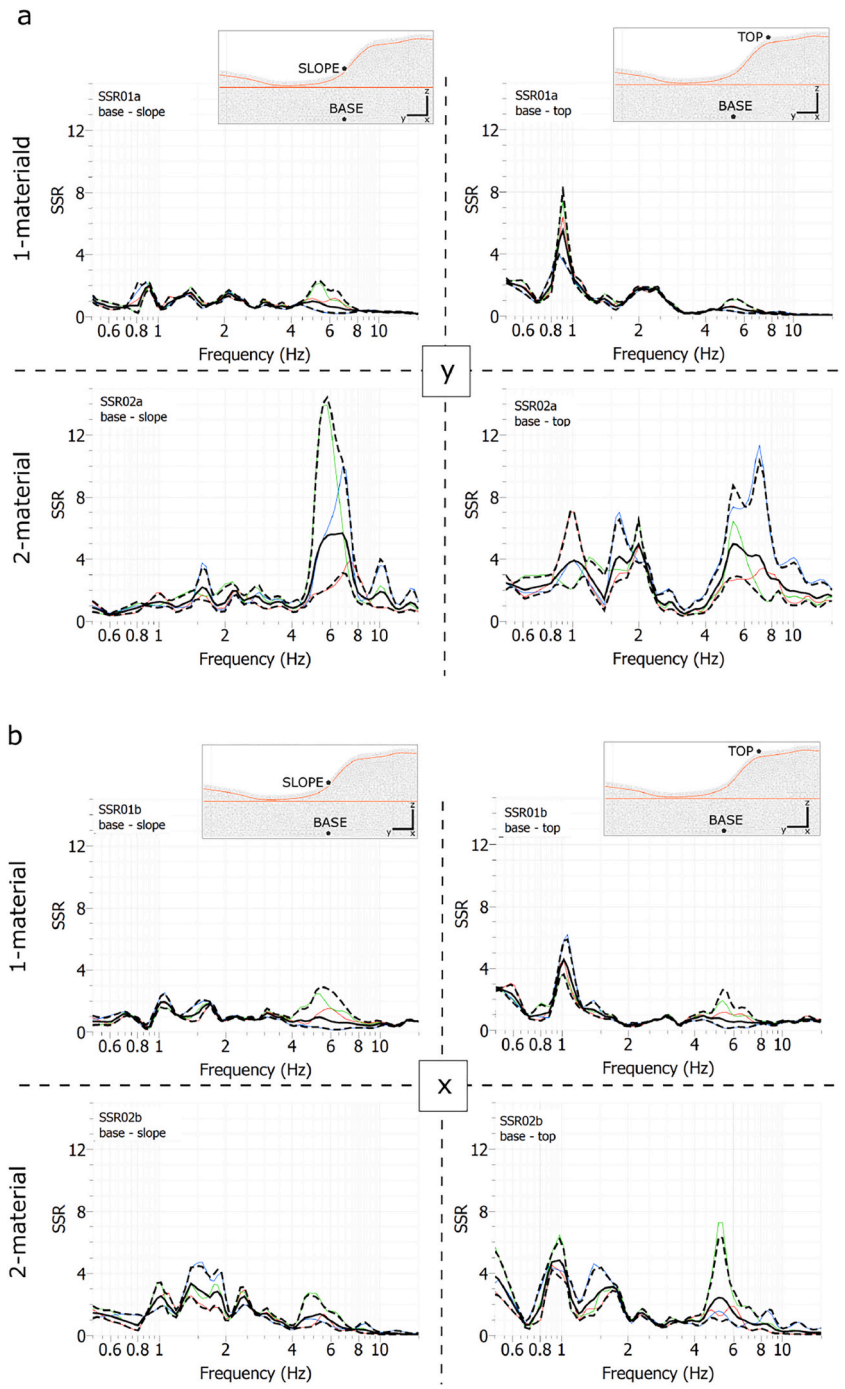

Fig. 10. Site effect analysis in the elastic domain: (a) y-orientated excitation and (b) x-orientated excitation for the 1-material (uniform bedrock) and 2-material (weaker near-surface material) models, respectively. The colored curves represent the frequency dependent amplification over constant time windows (5 to 10 seconds). The averaged amplification response is marked by the black curve and its standard deviation by the pointed lines, respectively.

field measurements. Furthermore, it is based on a realistic morphology reproducing neighbouring slope shapes that are not affected by landsliding. In addition, seismic wave transmission and amplification tests could show the validity of the model domain by numerically reproducing seismic site effects similar to those measured at the in-situ rock above the source zone of the landslide.

The geomechanical approach to simulate failure development of the Balta slope (including simulated internal fracturing of rock mass) is principally based on measurements and field observations, i.e. the structural setting of the flysch bedrock, the fracture degree of landslide debris, the elasto-plastic properties as well as the fair to poor rock quality of in-situ rock. Even though we allow for internal fracturing of rock, in the dynamic domain, we observe a failure development that is predominated along the discontinuities cutting through the rock mass and the modelled sliding surface. This can be due to the tetrahedral form of the model elements constituting the rock mass; once the rock mass is mobilized, an internal fracturing of rock mass can be noted. However, observations on co-seismic rockslides in Central Asia by ("succession of debris layers", e.g., in the Kokomeren River valley Strom, 2010) could show a similar sequential deposition mechanism of landslide mass, supposedly guided by discontinuities such as joints or rock stratigraphy. The impact of modelled joint dip angle and orientation is further

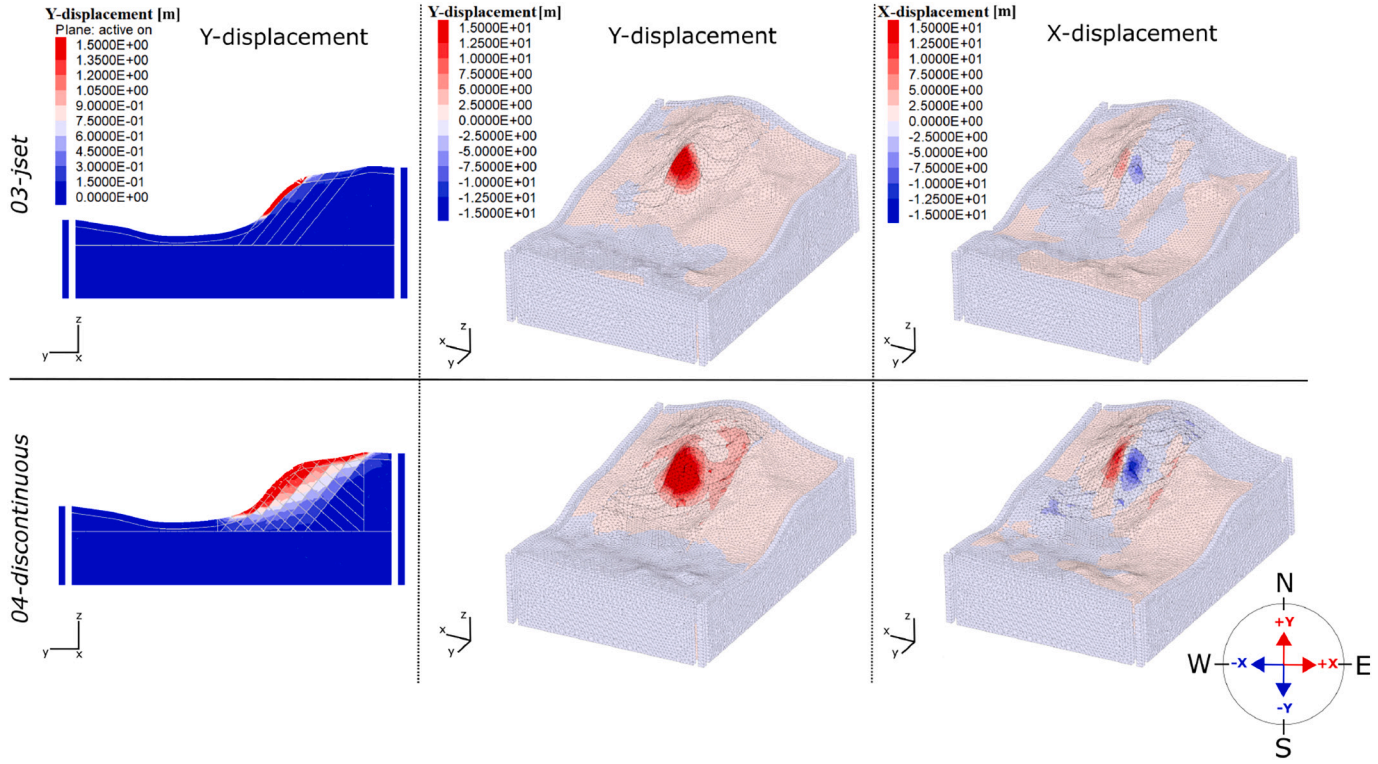

Fig. 11. Y- and x-displacement of blocks after 14 seconds of dynamic loading with the Ricker multiplier for the jset model configuration (*03-jset*; see Fig. 6c) and the jset-bedding model configuration (*04-discontinuous*; see Fig. 6d).

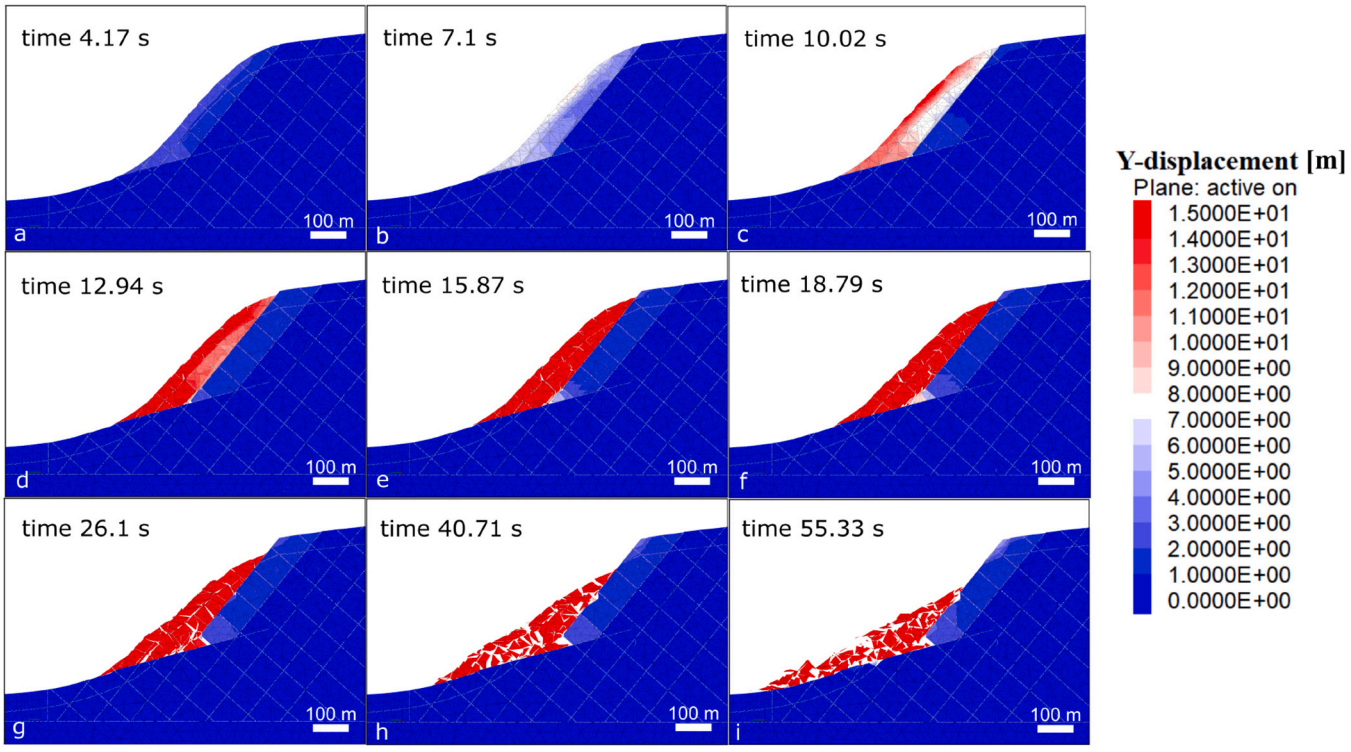

Fig. 12. Cross section showing Y-displacement contours of blocks during dynamic loading with Ricker wavelet; duration of dynamic load is 14 simulated seconds, i.e. landslide triggering (a-d), and residual block motion after seismic shaking (e-i).

outlined by the parametrical studies of the Balta slope in the 2D domain presented in Lemaire et al. (2020), where it is shown that the displacement pattern of seismically induced motion strongly depends on the defined structures. The actual case of Balta, as implemented in this work (with 55° anti-dip slope bedding and counter cutting joint planes), is marked by a lenticular displacement contour indicating rotational

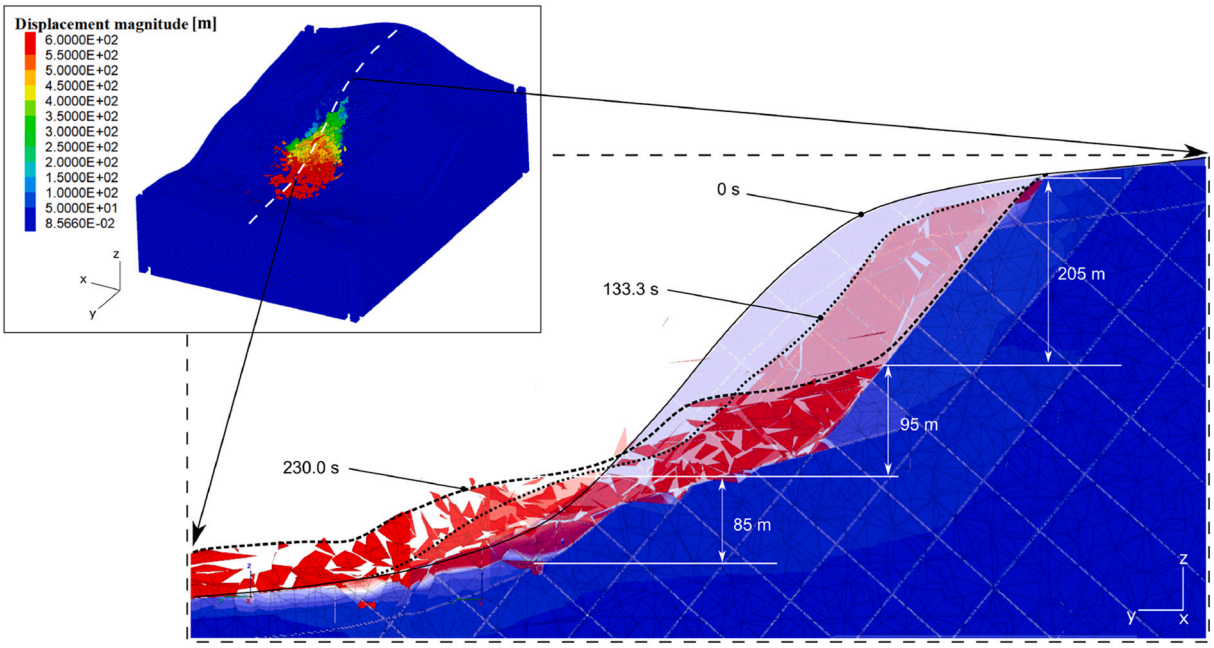

Fig. 13. Simulation of the Balta failure after 0, 133.3 and 230 simulated seconds (of which the first 120 s account for dynamic loading with the 2014 Iquique signal) shown on a central cross section. The inset figure shows the location of the cross section and the total displacement magnitude [m] of blocks after 230 simulated seconds.

sliding. A failure shape even closer to the actual state could possibly be produced by implementing more closely spaced joint planes, however this solution would significantly increase the related computational effort and was not feasible in the frame of this work.

For the Iquique earthquake simulation, the general block motion is directed towards the valley; however, the x-component of block displacements demonstrates a 3D effect probably due to the morphology of the modelled pre-failure slope topography and the combined x-y-orientated stress induced at the model bottom. This effect causes lateral expansion of landslide debris to a broader extent than the source zone width at the relatively narrow head scarp - a result that is in accordance with the actual post-failure debris distribution apparent in our study area. Subsequently to the period of ground acceleration, the run-out kinematics of the material are driven by the residual block velocity leading to mass movement during an extended period of time.

In terms of travel distance, the debris mass reaches the valley bottom after the modelled 230 seconds; considering the rapid and voluminous failure, the Balta rockslide could possibly have caused the blockage of the river. As mentioned in the study area description, the opposite slope of Balta was also subject to former landsliding, which in case of simultaneous triggering, could even have led to the formation of a temporary barrier lake in the valley. As the computed slope behaviour shows a layered detachment of rock along the modelled joint planes, we conclude that the debris reaching the valley originates from the upper surface-near slope layers, and is supposedly marked by a high fracture degree due to the long travel distance (>500 m) from depletion to accumulation zone. Rock layers located in more profound depths only initiate significant motion after the collapse of the former. The source zone of the rock mass forming the *plateau* area is thus supposedly located in the inner slope as demonstrated by the models; according to our geophysical prospections (see Mreyen et al., 2021), the rock mass might consequently be less fractured due to the relatively higher rock strength at the inner slope, as well as the limited travel distance to the depositional area (supposedly caused by the increasing friction of rockslide debris along the rupture surface and related kinetic energy loss).

Our numerical modelling results provide valuable insights in the kinematics and possible processes implicated in the landslide development. While the morphological shape of the actual Balta slope could be simulated close to the observed one, it could not be entirely reproduced (especially in terms of scarp height and depth). As mentioned above, more detailed structural modelling, e.g. closer and more numerous joint planes, could possibly increase post-failure accuracy. Another key element to be discussed in this regard is the possible effect of soil moisture and groundwater in the pre-failure slope, that supposedly could have an important impact on dynamic modelling results due to elevated water pressures. This latter aspect was not considered due to the computational complexity of the 3D dynamic domain, but also the uncertainty related to the local pre-historic groundwater regime given the advanced age of the landslide. Indeed, the region of the Flysch Carpathians is marked by a humid continental climate and the aspect of groundwater fluctuations, potentially reducing slope stability of the area significantly, should not be neglected. Still, we suggest that extensive rainfall periods and elevated water saturation cannot be considered as unique trigger factors for the deep-seated Balta slope failure, as these climatic phenomena typically cause rather superficial slides and flows in the region. Based the numerical analyses presented in this work, we consider one or multiple seismic events, possibly combined with climatic factors (long- to short-term), to be at the origin of the Balta slope failure.

7. Conclusions

The pre-historic Balta rockslide in the seismically active part of the Romanian Carpathian Mountains was back-modelled to pre-failure conditions in terms of topographical, structural and geomechanical settings and introduced to a 3D distinct element environment. Static analyses showed that the estimated pre-failure slope is stable under gravitational loads. Seismic shaking was modelled with a synthetic Ricker wavelet and a real earthquake record of a Chilean subduction event; the introduced signals are characterized by PGA values of 0.1–0.2 g at the model surface in x- and y-directions, and produce frequency peaks of 1.2–2.5 Hz at the hill crest (a frequency range that was also measured by actual seismic tests above the slope crown). The reproduction of slope failure could be initiated with the implementation of a rupture surface at the landslide base and dynamic loading of the slope. The sliding motion is predominately guided by the implemented joint

planes, while internal failure of rock mass initiates in form of brittle fracturing after the triggering of block motion by seismic shaking. During this back-analysis, specific morphological markers, such as the landslide scarp and central *plateau* area, could be reproduced; the material reaches the valley with maximum displacements of approximately 1350 m and the debris distribution is marked by a lateral spread. Provided that the chosen pre-failure model approximates real conditions, our analyses show a probable co-seismic development of the Balta slope. Future analyses will explore in greater detail the characteristic seismicity of the region using representative earthquake records of the investigated area. By this, we might extend our studies to other prehistoric slope instabilities in the valleys of Vrancea-Buzau and the Carpathian mountains, constituting valuable new information for future seismic hazard estimations of the region.

Credit author statement

Role of the authors: Anne-Sophie Mreyen - Conceptualization, Data curation, Investigation, Methodology, Visualization, Writing - original draft, review & editing; Davide Donati - Methodology, Software, Validation, Writing - review & editing; Davide Elmo - Methodology, Software, Validation, Writing - review & editing; Frederic Victor Donze - Software, Validation, Writing - review & editing; Hans-Balder Havenith - Conzeptualization, Funding acquisition; Supervision; Writing - review & editing.

Declaration of Competing Interest

The authors declare that they have no known competing financial interests or personal relationships that could have appeared to influence the work reported in this paper.

Acknowledgements

This research was partly funded by the WBI (Wallonie - Bruxelles International, with the bilateral project *'Evaluation des risques long-termes liés aux mouvements de masse déclenchés par les séismes dans la région de Vrancea, Roumanie'*), as well as by the F.R.S-FNRS Belgium in the frame of the FNRS-SNF collaboration project '4D seismic response and slope failure'. We further acknowledge the FRIA-FNRS research fellowship granted to Anne-Sophie Mreyen during the years 2016–2020. Finally, we thank the editor and the reviewers for their helpful suggestions that improved the quality of this work.

References

Bathe, K.-J., Ramm, E., Wilson, E.L., 1975. Finite element formulations for large deformation dynamic analysis. Int. J. Numer. Method Eng. 9 (2), 353–386.
Biggs, J., 1964. Introduction to Structural Dynamics. McGraw-Hill College, New York, USA.
Bokelmann, G., Rodler, F.-A., 2014. Nature of the Vrancea seismic zone (Eastern Carpathians)-new constraints from dispersion of first-arriving P-waves. Earth Planet. Sci. Lett. 390, 59–68.
Bonilla-Sierra, V., Scholtes, L., Donzé, F., Elmouttie, M., 2015. Rock slope stability analysis using photogrammetric data and DFN-DEM modelling. Acta Geotech. 10 (4), 497–511.
Bourdeau, C., Havenith, H.-B., 2008. Site effects modelling applied to the slope affected by the suusamyr earthquake (Kyrgyzstan, 1992). Eng. Geol. 97 (3–4), 126–145.
Bozzano, F., Lenti, L., Martino, S., Montagna, A., Paciello, A., 2011. Earthquake triggering of landslides in highly jointed rock masses: reconstruction of the 1783 scilla rock avalanche (Italy). Geomorphology 129 (3–4), 294–308.
Bozzano, F., Lenti, L., Martino, S., Paciello, A., Scarascia Mugnozza, G., 2008. Self-excitation process due to local seismic amplification responsible for the reactivation of the salcito landslide (Italy) on 31 october 2002. J. Geophys. Res.: Solid Earth 113, B10.
Burjánek, J., Edwards, B., Fäh, D., 2014. Empirical evidence of local seismic effects at sites with pronounced topography: a systematic approach. Geophys. J. Int. 197 (1), 608–619.
Burjánek, J., Gischig, V., Moore, J.R., Fäh, D., 2018. Ambient vibration characterization and monitoring of a rock slope close to collapse. Geophys. J. Int. 212 (1), 297–310.
Burjánek, J., Kleinbrod, U., Fäh, D., 2019. Modeling the seismic response of unstable rock mass with deep compliant fractures. J. Geophys. Res.: Solid Earth 124 (12), 13039–13059.
Che, A., Yang, H., Wang, B., Ge, X., 2016. Wave propagations through jointed rock masses and their effects on the stability of slopes. Eng. Geol. 201, 45–56.
Crozier, M., 1992. Determination of palaeoseismicity from landslides.. In: In International Symposium on Landslides, pp. 1173–1180.
Cundall, P., 1976. Explicit finite differnce method in geomechanics. Second Int. Conf. Numerical Methods in Geomechanics, Blacksburg, 1976. volume 1, pp. 132–150.
Cundall, P., Hansteen, H., Lacasse, S., Selnes, P., 1980. NESSI, soil structure interaction program for dynamic and static problems. Norwegian Geotech. Inst. Rep. 9, 51508–51509.
Dawson, E., Roth, W., Drescher, A., 1999. Slope stability analysis by strength reduction. Geotechnique 49 (6), 835–840.
Del Gaudio, V., Zhao, B., Luo, Y., Wang, Y., Wasowski, J., 2019. Seismic response of steep slopes inferred from ambient noise and accelerometer recordings: the case of dadu river Valley, China. Eng. Geol. 259, 105197.
Donati, D., Stead, D., Elmo, D., Karimi Sharif, L., Gao, F., Borgatti, L., Spreafico, M., 2018. Experience gained in modelling brittle fracture in rock. 52nd US Rock Mechanics/Geomechanics Symposium. OnePetro..
Dragotă, C.S., 2006. Precipitaţiile excedentare în România, edit, Academiei Române, Bucureşti, pp. 53–57.
Georgescu, E., 2002. The partial collapse of Coltzea Tower during the Vrancea earthquake of 14/26 october 1802: the historical warning of long-period ground motions site effects in Bucharest. International Conference Earthquake Loss Estimation and Risk Reduction.
Georgescu, E.-S., Pomonis, A., 2012. Building damage vs. territorial casualty patterns during the Vrancea (Romania) earthquakes of 1940 and 1977. 15th World Conference on Earthquake Engineering, pp. 24–28.
Gholamy, A., Kreinovich, V., 2014. Why Ricker wavelets are successful in processing seismic data: towards a theoretical explanation. 2014 IEEE Symposium on Computational Intelligence for Engineering Solutions (CIES). IEEE, Orlando, Florida, USA, pp. 11–16.
Gischig, V., Eberhardt, E., Moore, J., Hungr, O., 2015. On the seismic response of deep-seated rock slope instabilities— insights from numerical modeling. Eng. Geol. 193, 1–18.
Gischig, V., Preisig, G., Eberhardt, E., 2016. Numerical investigation of seismically induced rock mass fatigue as a mechanism contributing to the progressive failure of deep-seated landslides. Rock Mech. Rock Eng. 49 (6), 2457–2478.
Havenith, H.-B., Jongmans, D., Faccioli, E., Abdrakhmatov, K., Bard, P.-Y., 2002. Site effect analysis around the seismically induced Ananevo rockslide, Kyrgyzstan. Bull. Seismol. Soc. Am. 92 (8), 3190–3209.
Havenith, H.-B., Strom, A., Calvetti, F., Jongmans, D., 2003a. Seismic triggering of landslides. Part B: simulation of dynamic failure processes. Nat. Hazards Earth Sys. Sci. 6, 663–682.
Havenith, H.-B., Vanini, M., Jongmans, D., Faccioli, E., 2003b. Initiation of earthquake-induced slope failure: influence of topographical and other site specific amplification effects. J. Seismol. 7 (3), 397–412.
He, J., Qi, S., Wang, Y., Saroglou, C., 2020. Seismic response of the lengzhuguan slope caused by topographic and geological effects. Eng. Geol. 265, 105431.
Huang, R., Pei, X., Fan, X., Zhang, W., Li, S., Li, B., 2012. The characteristics and failure mechanism of the largest landslide triggered by the wenchuan earthquake, may 12, 2008, China. Landslides 9 (1), 131.
Hungr, O., Evans, S., 2004. Entrainment of debris in rock avalanches: an analysis of a long run-out mechanism. Geol. Soc. Am. Bull. 116 (9–10), 1240–1252.
Hungr, O., Leroueil, S., Picarelli, L., 2014. The Varnes classification of landslide types. Update Landslid. 11 (2), 167–194.
Itasca, 2016. 3DEC— Three-Dimensional Distinct Element Code (Version 5.2).
Itasca, 2019. Griddle (Version 1.0).
Iverson, R.M., Reid, M.E., LaHusen, R.G., 1997. Debris-flow mobilization from landslides. Annu. Rev. Earth Planet. Sci. 25 (1), 85–138.
Jaboyedoff, M., Chigira, M., Arai, N., Derron, M.-H., Rudaz, B., Tsou, C.-Y., 2019. Testing a failure surface prediction and deposit reconstruction method for a landslide cluster that occurred during Typhoon Talas (Japan). Earth Surface Dyn. 7 (2), 439–458.
Jibson, R.W., 1996. Use of landslides for paleoseismic analysis. Eng. Geol. 43 (4), 291–323.
Keefer, D.K., 1984. Landslides caused by earthquakes. Geol. Soc. Am. Bull. 95 (4), 406–421.
Khazai, B., Sitar, N., 2004. Evaluation of factors controlling earthquake-induced landslides caused by Chi-Chi earthquake and comparison with the Northridge and Loma Prieta events. Eng. Geol. 71 (1–2), 79–95.
Kim, D.H., Gratchev, I., Balasubramaniam, A., 2015. Back analysis of a natural jointed rock slope based on the photogrammetry method. Landslides 12 (1), 147–154.
Knapp, J.H., Knapp, C.C., Raileanu, V., Matenco, L., Mocanu, V., Dinu, C., 2005. Crustal constraints on the origin of mantle seismicity in the vrancea zone. romania: the case for active continental lithospheric delamination. Tectonophysics 410 (1–4), 311–323.
Kuhlemeyer, R.L., Lysmer, J., 1973. Finite element method accuracy for wave propagation problems. J. Soil Mech. Found. Div 99(Tech Rpt). 95 (4), 859–877.
Lemaire, E., Mreyen, A.-S., Dufresne, A., Havenith, H.-B., 2020. Analysis of the influence of structural geology on the massive seismic slope failure potential supported by numerical modelling. Geosciences 10 (8), 323.
Li, L.-q., Ju, N.-p., Zhang, S., Deng, X.-x., Sheng, D., 2019. Seismic wave propagation characteristic and its effects on the failure of steep jointed anti-dip rock slope. Landslides 16 (1), 105–123.

Luo, J., Pei, X., Evans, S.G., Huang, R., 2019. Mechanics of the earthquake-induced hongshiyan landslide in the 2014 mw 6.2 ludian earthquake, Yunnan, China. Eng. Geol. 251, 197–213.
Luo, Y., Fan, X., Huang, R., Wang, Y., Yunus, A.P., Havenith, H.-B., 2020. Topographic and near-surface stratigraphic amplification of the seismic response of a mountain slope revealed by field monitoring and numerical simulations. Eng. Geol. 271, 105607.
Lysmer, J., Kuhlemeyer, R.L., 1969. Finite dynamic model for infinite media. J. Eng. Mech. Div. 95 (4), 859–878.
Mândrescu, N., 1981. The Romanian earthquake of march 4, 1977; aspects of soil behaviour, Revue roumaine de géologie, géophysique et géographie. Géophysique 25, 35–56.
Marinos, P., Hoek, E., 2001. Estimating the geotechnical properties of heterogeneous rock masses such as flysch, Bulletin of Eng. Geol. Env. 60 (2), 85–92.
Marinos, P., Hoek, E., et al., 2000. Gsi: a geologically friendly tool for rock mass strength estimation.. In: In ISRM International Symposium. International Society for Rock Mechanics and Rock Engineering.
Maufroy, E., Cruz-Atienza, V.M., Cotton, F., Gaffet, S., 2015. Frequency-scaled curvature as a proxy for topographic site-effect amplification and ground-motion variability. Bull. Seismol. Soc. Am. 105 (1), 354–367.
McNeel, R., et al., 2010. Rhinoceros 3d, Version 5. 0. Robert McNeel & Associates, Seattle, WA.
Meunier, P., Hovius, N., Haines, J.A., 2008. Topographic site effects and the location of earthquake induced landslides. Earth Planet. Sci. Lett. 275 (3–4), 221–232.
Micu, M., 2017. The systematic of landslide processes in the conditions of romania's relief. In: In Landform Dynamics and Evolution in Romania. Springer, pp. 249–269.
Micu, M., Bălteanu, D., Micu, D., Zarea, R., Raluca, R., 2013. Landslides in the Romanian curvature carpathians in 2010. In: In Geomorphological impacts of extreme weather. Springer, pp. 251–264.
Ministry of Environment, B., 2018. Raport anual privind Starea Mediului în Romania pe anul 2018. Ministerul Mediului Bucuresti 1–678. http://www.anpm.ro/raport-de-mediu.
Moore, J.R., Gischig, V., Burjanek, J., Loew, S., Fäh, D., 2011. Site effects in unstable rock slopes: dynamic behavior of the randa instability (switzerland). Bull. Seismol. Soc. Am. 101 (6), 3110–3116.
Mreyen, A.-S., Cauchie, L., Micu, M., Onaca, A., Havenith, H.-B., 2021. Multiple geophysical investigations to characterize massive slope failure deposits: application to the Balta rockslide, Carpathians. Geophys. J. Int. 225 (2), 1032–1047.
Pal, S., Kaynia, A.M., Bhasin, R.K., Paul, D., 2012. Earthquake stability analysis of rock slopes: a case study. Rock Mech. Rock Eng. 45 (2), 205–215.
Pi na-Valdés, J., Socquet, A., Cotton, F., Specht, S., 2018. Spatiotemporal variations of ground motion in northern Chile before and after the 2014 Mw 8.1 Iquique megathrust event. Bulletin of the Seismological Society of America 108 (2), 801–814.
Radu, C., Spânoche, E., 1977. On geological phenomena associated with the 10 november 1940 earthquake. Revenue Rom. Geol. Geophys. et Geograph. Geophys. 21, 159–165.
Radulescu, N.A., 1941. Considérations géographiques sur le tremblement de terre du 10 november 1940. Comptes Rendus de Séances de LAcadémie des Sciences de Roumanie 5 (3), 243–269.
Radulian, M., Bala, A., Popescu, E., Toma-Danila, D., 2018. Earthquake mechanism and characterization of seismogenic zones in south-eastern part of Romania. Annal. Geophys. 61 (1), SE108–SE109.
Ricker, N., 1953. The form and laws of propagation of seismic wavelets. Geophysics 18 (1), 10–40.
Rocscience, 2002. RocLab (Version 1.0) - Rock Mass Strength Analysis using the Generalized Hoek-Brown Failure Criterion.
Rogozea, M., Marmureanu, G., Radulian, M., Toma, D., 2014. Reevaluation of the macroseismic effects of the 23 january 1838 Vrancea earthquake. Rom. Rep. Phys. 66 (2), 520–538.
Romeo, R., 2000. Seismically induced landslide displacements: a predictive model. Eng. Geol. 58 (3–4), 337–351.
Sassa, K., 1996. Prediction of earthquake induced landslides.. In: In Landslides, pp. 115–132.
Scholtès, L., Donzé, F.V., 2015. A dem analysis of step-path failure in jointed rock slopes. Comptes Rendus Mécanique 343 (2), 155–165.
Seequent, 2021. Leapfrog Geo.
Sepúlveda, S.A., Murphy, W., Jibson, R.W., Petley, D.N., 2005. Seismically induced rock slope failures resulting from topographic amplification of strong ground motions: the case of pacoima Canyon, California. Eng. Geol. 80 (3–4), 336–348.
Singeisen, C., Ivy-Ochs, S., Wolter, A., Steinemann, O., Akçar, N., Yesilyurt, S., Vockenhuber, C., 2020. The Kandersteg rock avalanche (Switzerland): integrated analysis of a late Holocene catastrophic event. Landslides 6, 1–21.
Song, D., Chen, Z., Chao, H., Ke, Y., Nie, W., 2020. Numerical study on seismic response of a rock slope with discontinuities based on the time-frequency joint analysis method. Soil Dyn. Earthquake Eng. 133, 106112.
Stead, D., Wolter, A., 2015. A critical review of rock slope failure mechanisms: the importance of structural geology. J. Struct. Geol. 74, 1–23.
Strom, A., 2010. Landslide dams in central asia region. J. Jap. Lands. Soc. 47 (6), 309–324.
USGS, 2020. U.G.S. Earthquake Hazards - Event Page.
Vacareanu, R., Ionescu, C., 2016. The 1940 Vrancea Earthquake. Issues, Insights and Lessons Learnt: proceedings of the symposium Commemorating 75 Years from November 10, 1940 Vrancea Earthquake. Springer, Bucharest, Romania.
Wang, G., Sassa, K., 2003. Pore-pressure generation and movement of rainfall-induced landslides: effects of grain size and fine-particle content. Engineering geology 69 (1–2), 109–125.
Wang, G., Sassa, K., 2009. Seismic loading impacts on excess pore-water pressure maintain landslide triggered flowslides. Earth Suface Proc. Landforms 34 (2), 232–241.
Weber, S., Beutel, J., Häusler, M., Geimer, P.R., Fäh, D., Moore, J.R., 2022. Spectral amplification of ground motion linked to resonance of large-scale mountain landforms. Earth Planet. Sci. Lett. 578, 117295.
Willenberg, H., Loew, S., Eberhardt, E., Evans, K.F., Spillmann, T., Heincke, B., Maurer, H., Green, A.G., 2008. Internal structure and deformation of an unstable crystalline rock mass above randa (switzerland): part i—internal structure from integrated geological and geophysical investigations. Engineering Geology 101 (1–2), 1–14.
Zangerl, C., Chwatal, W., Kirschner, H., 2015. Formation processes, geomechanical characterisation and buttressing effects at the toe of deep-seated rock slides in foliated metamorphic rock. Geomorphology 243, 51–64.
Zhu, Y., Dai, F., Yao, X., Tu, X., Shi, X., 2019. Field investigation and numerical simulation of the seismic triggering mechanism of the Tahman landslide in eastern Pamir, Northwest China. Bull. Eng. Geol. Environ. 78 (8), 5795–5809.